LEVEL III (3)

MRDC41007.18AR

TEMPERATURE COMPENSATED PIEZOELECTRIC MATERIALS

Annual Technical Report No. 2
For Period 05/15/80 through 05/14/81

July, 1981

DTIC
ELECTE
FEB 9 1982
S H

The views and conclusions contained in this document are those of the authors
and should not be interpreted as necessarily representing the official policies,
either expressed or implied, of the Defense Advanced Research Projects Agency
or the United States Government.

82 02 08 065

REPORT DOCUMENTATION PAGE	READ INSTRUCTIONS BEFORE COMPLETING FORM

1. REPORT NUMBER AFOSR-TR- 82 -0004	2. GOVT ACCESSION NO. AD-A110 649	3. RECIPIENT'S CATALOG NUMBER

4. TITLE (and Subtitle) Temperature Compensated Piezoelectric Materials	5. TYPE OF REPORT & PERIOD COVERED Annual Technical Report #2 05/15/80 through 06/14/81
	6. PERFORMING ORG. REPORT NUMBER MRDC41007.18AR

7. AUTHOR(s) R. R. Neurgaonkar	8. CONTRACT OR GRANT NUMBER(s) F49620-78-C-0093

9. PERFORMING ORGANIZATION NAME AND ADDRESS Rockwell International Microelectronics Research & Development Center Thousand Oaks, CA 91360	61102F 3570/01

11. CONTROLLING OFFICE NAME AND ADDRESS Air Force Office of Scientific Research Bolling Air Force Base Washington, D.C. 20332	12. REPORT DATE July, 1981
	13. NUMBER OF PAGES 74

14. MONITORING AGENCY NAME & ADDRESS(if different from Controlling Office)	15. SECURITY CLASS. (of this report) Unclassified
	15a. DECLASSIFICATION/DOWNGRADING SCHEDULE

16. DISTRIBUTION STATEMENT (of this Report)

Approved for public release; distribution unlimited.

17. DISTRIBUTION STATEMENT (of the abstract entered in Block 20, if different from Report)

18. SUPPLEMENTARY NOTES

19. KEY WORDS (Continue on reverse side if necessary and identify by block number)

Strontium barium niobates	Gibb's energy functions
Liquid phase epitaxy	Phenomenological model
Czochralski growth technique	Elastic compliances

20. ABSTRACT (Continue on reverse side if necessary and identify by block number)

From the electrostriction measurements on SBN crystals, it was found that the fourth order electrostrictive coupling terms are not adequate to fully describe the parelectric phase above curie temperature, and hence six rank coupling terms are needed; the electrostrictive coupling terms do not change markedly with cation substitution. Several flux systems have successfully been developed for the liquid phase epitaxy work of SBN compositions. The work is successful, and it is possible to develop epilayers of SBN compositions using barium vanadate flux. SBN crystals grown in our laboratory were used

DD FORM 1 JAN 73 1473 EDITION OF 1 NOV 65 IS OBSOLETE

TABLE OF CONTENTS

Rockwell International

MRDC41007.18AR

LIST OF ILLUSTRATIONS

LIST OF ILLUSTRATIONS (Cont.)

LIST OF ILLUSTRATIONS (Cont.)

LIST OF TABLES

1.0 PROGRESS AND TECHNICAL SUMMARY

The Landau:Ginsburg:Devonshire phenomenological theory for the tungsten bronze family indicates that the sixth order Φ coupling leads to a dependence of the stiffened elastic compliances, s^P_{klmn}, on the polarization components, $P_i P_j$, which takes the simple form

$$s^P_{klmn}(P_i P_j) = s^P_{klmn}(0) + \Phi P_i P_j$$

where $s^P_{klmn}(P_i P_j)$ is the elastic compliance at the polarization level $P_i P_j$, and $s^P_{klmn}(0)$ is the compliance at constant and zero polarization. This phenomenological analysis has been applied to studies of the elastic behavior of ferroelectric bronze, $Sr_{.61}Ba_{.39}Nb_2O_6$. Direct measurements by induced piezoelectric resonance in the paraelectric phase clearly showed a coupling between the stiffened elastic compliances, s^P_{ij}, on induced electric polarization in a manner consistent with that predicted from the sixth order electrostriction. The sixth order Φ constants were used to predict the elastic behavior in the spontaneously polarized ferroelectric phase region. The observed behavior of the Φ constants was consistent with other higher constants, being only weakly temperature dependent and thus likely also compositionally independent.

Surface wave propagation has been theoretically and experimentally evaluated for the X, Z and (110) cuts of SBN:61. In addition, the temperature coefficient of delay has been evaluated over the range -20 to +50° C. Although these measurements indicate that this composition possesses temperature compensated orientations, SAW measurements show a hysteresis in delay during temperature cycling. Since these measurements have been obtained for only one boule, the results are incomplete to determine the source of the instability. In view of this fact, it is proposed to investigate the stability of SBN using several different available boules. Based on this information, it will be possible to identify the factors affecting stability, which may be associated with material growth, material characteristics or with acoustical measurement techniques. Now that material properties and SAW device characterization are becoming avail-

able, rapid improvements in crystal composition and quality can be accomplished to obtain optimal material parameter and device performance.

The liquid phase epitaxial (LPE) technique has been shown to be successful for developing the $Sr_{.5}Ba_{.5}Nb_2O_6$ type bronze films onto the various orientations such as (100), (110) and (001) of the $Sr_{.61}Ba_{.39}Nb_2O_6$ substrates. Although the results of this investigation show that the growth is successful on all the orientations, it is much faster on the Z-plate. This observation is consistent with our results on the bulk single crystal growth of the composition $Sr_{.61}Ba_{.39}Nb_2O_6$ where the growth was only possible along the (001) direction. The quality of the films is reasonably good, and the films as thick as 50-60 μm have successfully been developed for acoustical and ferroelectric characterization. For successful acoustical measurements it is essential to obtain single domain films. It is therefore necessary, before measurements can be performed, to pole these films. This work is in progress and, once this is accomplished, it will be possible to obtain acoustical as well as piezoelectric data on these films.

A crystal of $Sr_{.61}Ba_{.39}Nb_2O_6$ supplied by Rockwell was optically evaluated at the Optical Technical Branch, Naval Research Laboratory. The results of this investigation showed that the SBN single crystal had better optical properties than $LiNbO_3$ or $LiTaO_3$; these measurements therefore appear promising for future work in this family. The half-wave voltage for this crystal was established at NRL and is estimated to be 300 V, about a factor 10 less than for $LiNbO_3$ or $LiTaO_3$.

2.0 PHENOMENOLOGICAL THEORY

2.1 Introduction

Earlier studies both on this contract and elsewhere have shown that compounds within the very extensive family of simple ferroelectric tungsten bronzes have properties which are interesting for acoustic wave device applications. The development of effective liquid phase hetero-epitaxy techniques on this contract now makes it possible to grow highly perfect striation-free films of both simple and multicomponent bronze solid solutions.

The purpose of the phenomenological theoretical studies on this program is to provide the theoretical basis for making intelligent selection among the vast family of property combinations which have thus been made available. The logic which mandates the phenomenological approach runs as follows.

1. To ascertain the potential utility of the bronze crystal of any particular composition, it is necessary to know for the poled single domain state:
   (a) the dielectric permittivity tensor
   (b) the piezoelectric tensor
   (c) the elastic compliance tensor
   (d) the thermal expansion tensor
   (e) the temperature derivations of all the above tensor coefficients.

   Clearly iterating measurements of all these parameters across the total family is an impossibly time consuming task.

2. Because of the complexity of the bronze structure and the difficulty of obtaining exact site occupancy data for the cation population, it is impossible to derive atomistic models from which it would be possible to calculate the elasto-dielectric properties and their temperature course.

3. Our extension of the Landau:Ginsburg:Devonshire formulation has indicated quite clearly that the sixth order electrostriction

parameter Φ_{ijklmn} play a most important role in the temperature dependence of the elastic compliances in the single domain ferroelectric state.

From measurements of the Φ parameters in the high temperature pyroelectric phase of a $Sr_{.61}Ba_{.39}Nb_2O_6$ bronze crystal, we are able to demonstrate temperature independence for these constants and to derive the lower temperature elastic compliances in the single domain ferroelectric phase..

4. Taken with the fact that the LGD method is able to predict both dielectric and piezoelectric response and "spontaneous strain" (thermal expansion), the method is capable of predicting the full family of required elasto-dielectric parameters from a very limited family of temperature independent higher order parameters of the prototypic paraelectric phase.

2.2 Progress in Modeling Studies

In the modeling studies to date, the following progress has been made.

1. The full LGD elastic Gibbs function has been developed, including all cross terms up to sixth order.

2. Solutions for the spontaneous electric polarization, the dielectric response, the spontaneous strain and the piezoelectric response have been developed for both the single domain tetragonal and orthorhombic simple ferroelectric states.

3. For the elastic response, it is shown that the stiffened compliances S_{ij}^p depend directly on the square of the polarization level through the sixth order Φ constants.

4. Using single crystals of the bronze composition $Sr_{.61}Ba_{.39}Nb_2O_6$ supplied from Rockwell, the full family of Φ_{3ij} constants needed to characterize the elastic response in the tetragonal polar single

domain state have been measured from the change in the stiffened compliance S_{ij}^P under DC bias induced polarization at a temperature above T_c (Figs. 1,2). By repeating such measurements for a range of temperatures above T_c on cuts of different orientation, the near temperature independence of the Φ_{3ij} was demonstrated (Fig. 3) and the values for Φ constants given in Table 1 determined.

5. From the measured spontaneous polarization P_s vs. T (Fig. 4) and the dielectric compliances K_3 and K_1 (Figs. 5,6), the thermodynamic stiffness parameters of Table 2 were determined. For these parameters, the fit between measured and calculated permittivities is shown in Figs. 7 and 8. Using a Q_{33} value of 0.34 m^4/c^2, the fit between measured and calculated thermal expansion vs. T is shown in Fig. 9.

6. Using again the SBN 61:39 crystals and the resonance method, elastic complicances S_{11}^P, S_{12}^P, S_{33}^P, S_{44}^P and S_{66}^P were measured through the single domain ferroelectric temperature range and compared to the values calculated using the thermodynamic parameters in Tables 1 and 2.

    Typical data for S_{12}^P are summarized in Fig. 10 and for S_{44}^P in Fig. 11. Experimental and calculated temperature coefficients of compliance are given in Table 3.

2.3 Discussion

From the very extensive work briefly summarized in the results presented above, it is clear that the thermodynamic phenomenology gives very good quasi-quantitative agreement with the measured elasto-dielectric parameters in SBN 61:39, except for temperatures very close to the Curie region T_c.

For the elastic compliance S_{44}^P, the material clearly stiffens with increasing temperature so that a temperature compensated cut for SAW propagation should be possible and has now been confirmed.

Particularly for the compliance S_{33}^P there is, however, an anomalous elastic compliance maximum in the vicinity of the Curie maximum of the dielec-
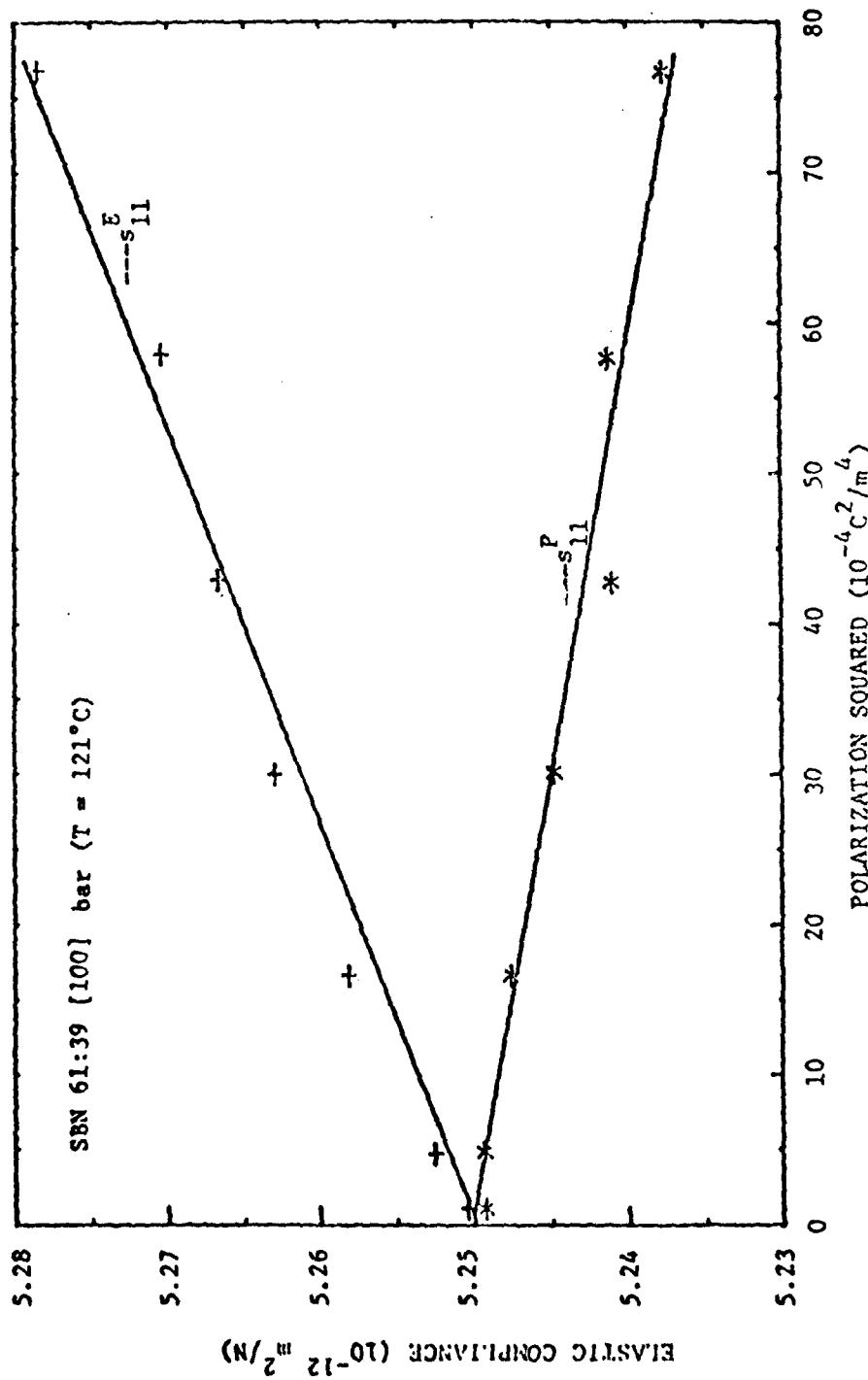
MRDC41007.18AR

Fig. 1. Elastic compliances s_{11}^E and s_{11}^P as a function of induced polarization in SBN 61:39 measured at 121°C.
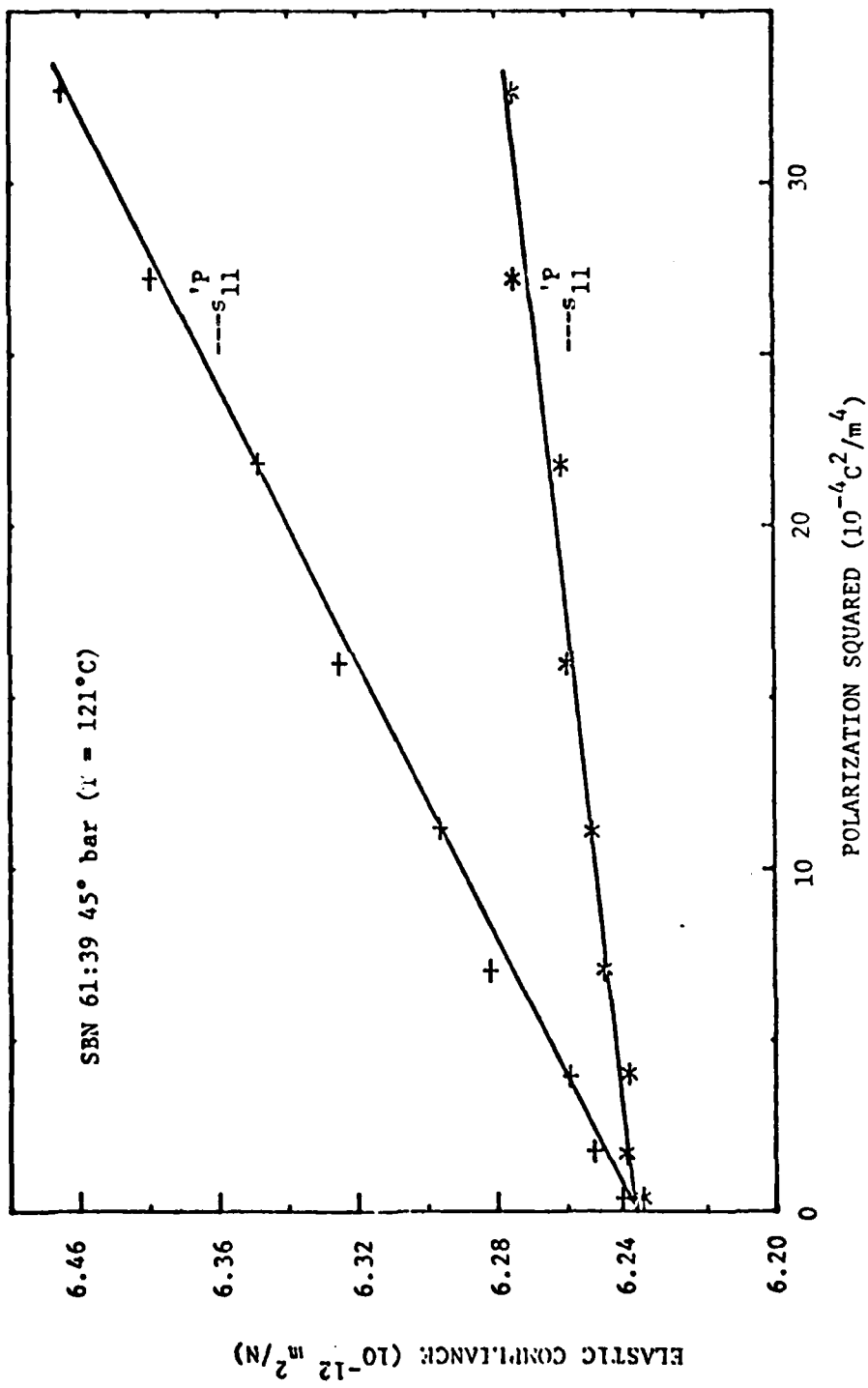
Fig. 2. Elastic compliances $s_{11}^{'E}$ and $s_{11}^{'P}$ as a function of induced polarization in SBN 61:39 measured at 121°C.
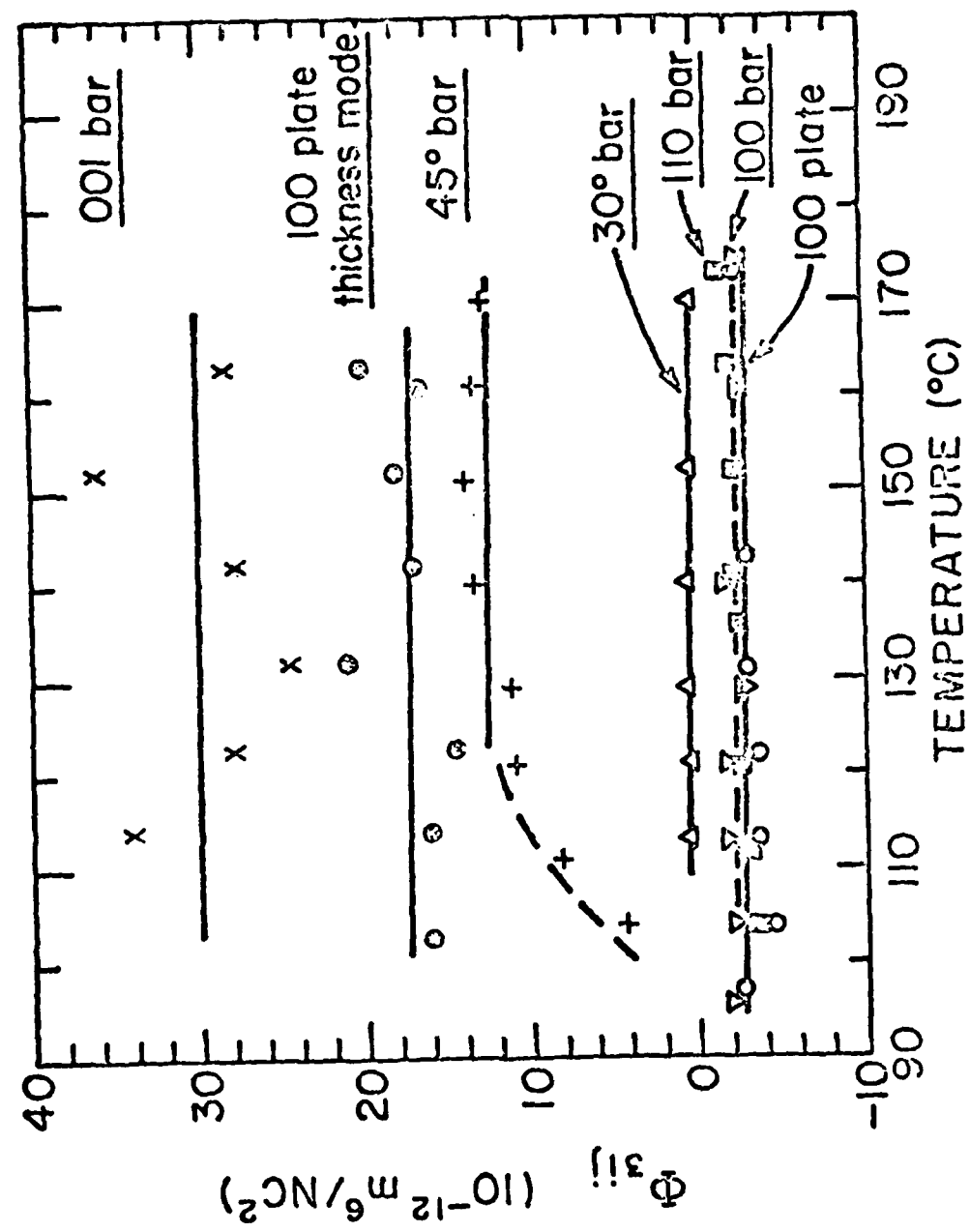
MRDC41007.18AR

Fig. 3. Measured sixth order electrostriction Φ_{3ij} values of rotated and unrotated cuts over a range of temperature above T_c.

TABLE 1

Higher Order Electrostriction Constants Φ_{3ij}

Φ_{311}	-2.2×10^{-12} m^6/N-coul^2
Φ_{312}	-3
Φ_{313}	-5
Φ_{333}	$+28$
Φ_{334}	$+35$ $*+(16)$
Φ_{366}	-3

* The higher order Φ_{334} constant determined from the 30° bar. Believed to be the truer value, since less dependent on possible "anomalous" behavior found in the (001) polar direction.
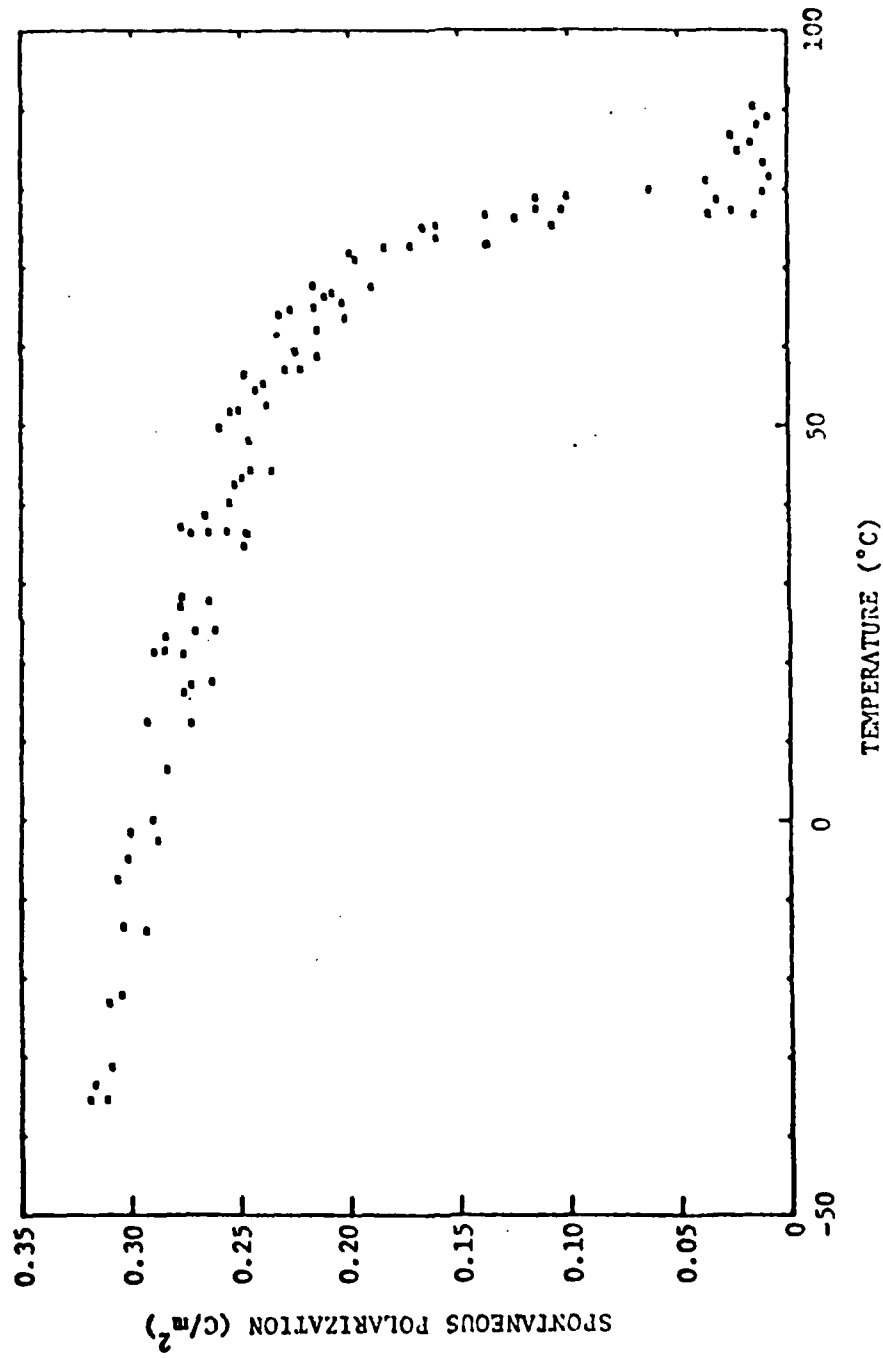
MRDC41007.18AR

Fig. 4. Temperature dependence of the spontaneous polarization in SBN 61:39.
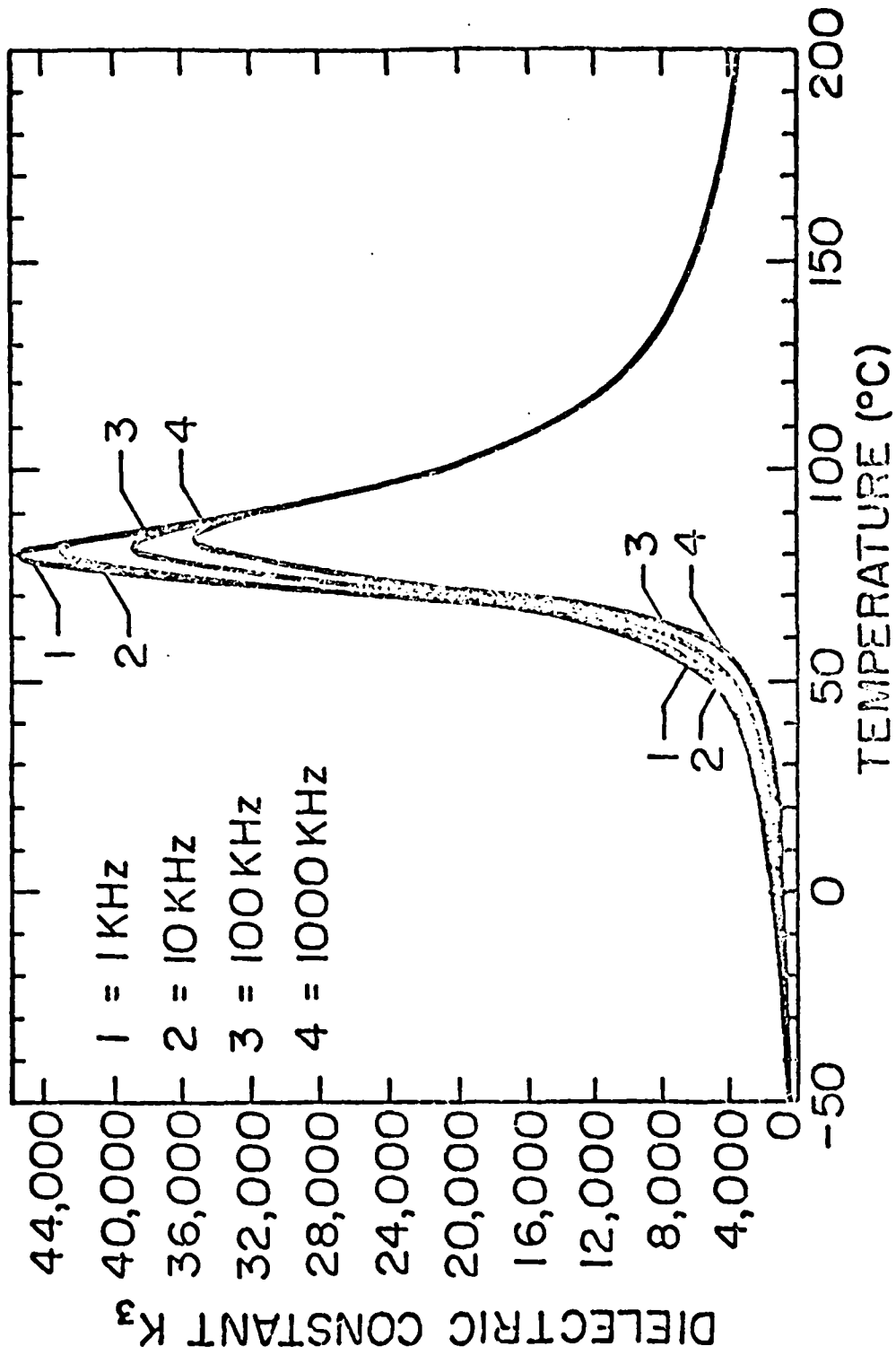
MRDC41007.18AR

Fig. 5.   Dielectric constants K_3 as a function of temperature and frequency for SBN 61:39.
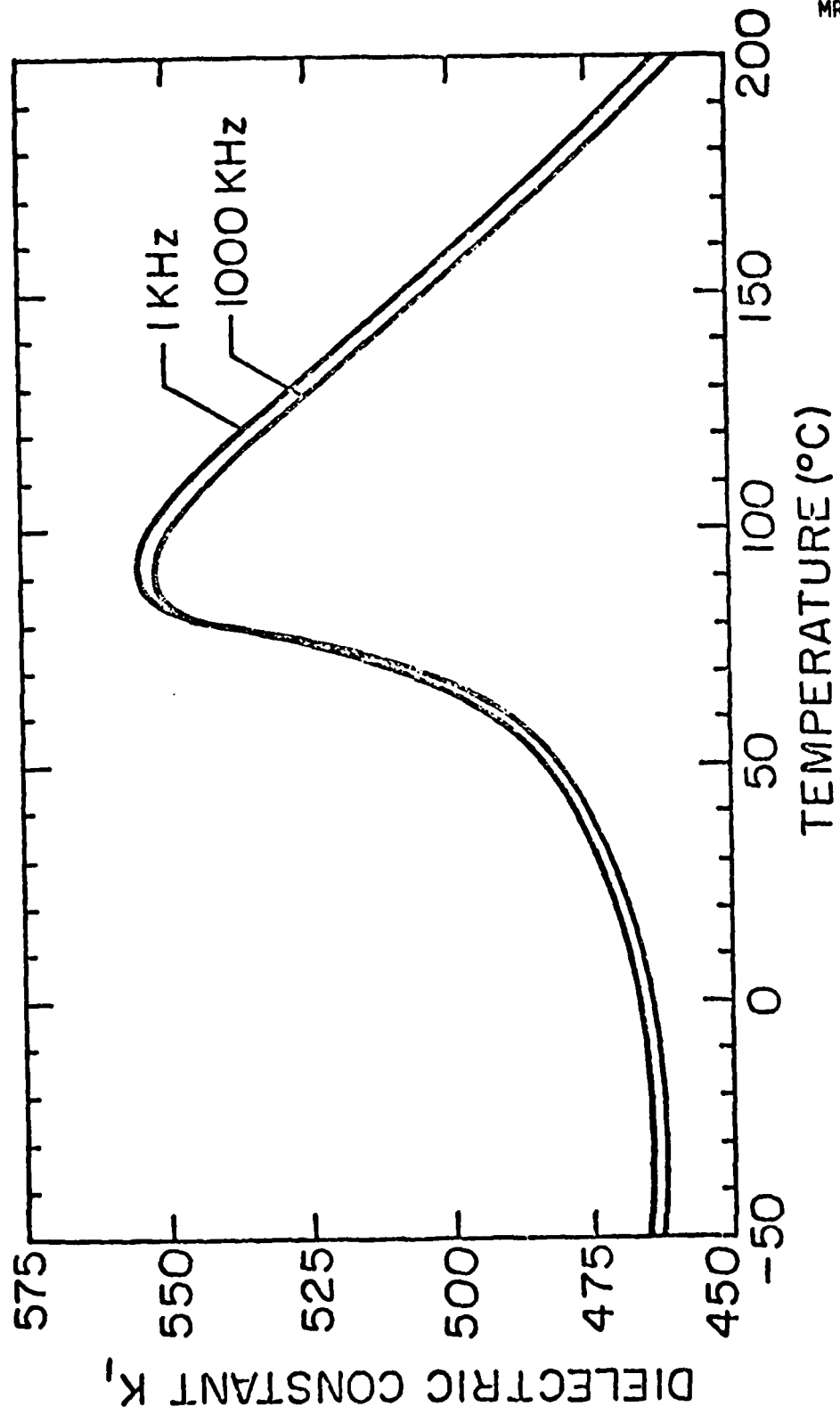
MRDC41007.18AR

Fig. 6. Dielectric constant K_1 as a function of temperature and frequency for SBN 61:39.

TABLE 2

Determined Thermodynamic Stiffness Parameters for SBN 61:39

$$\tfrac{1}{2}\alpha_{10} = 3.73 \times 10^{-6}/^\circ C \cdot \epsilon_o$$

$$\tfrac{1}{2}\alpha_{30} = 2.52 \times 10^{-6}/^\circ C \cdot \epsilon_o$$

$$\Theta_1 = -379^\circ C$$

$$\Theta_3 = 73^\circ C$$

$$\overline{T}_c = 77^\circ C$$

$$2\alpha_{13} = 4.2 \times 10^{-3} \text{ MKS}$$

$$2\alpha_{133} = 4.22 \times 10^{-2}$$

$$2\alpha_{1333} = 4.98 \times 10^{-2}$$

$$12\alpha_{33} = -8.4 \times 10^{-3}$$

$$30\alpha_{333} = 3.6 \times 10^{-1}$$
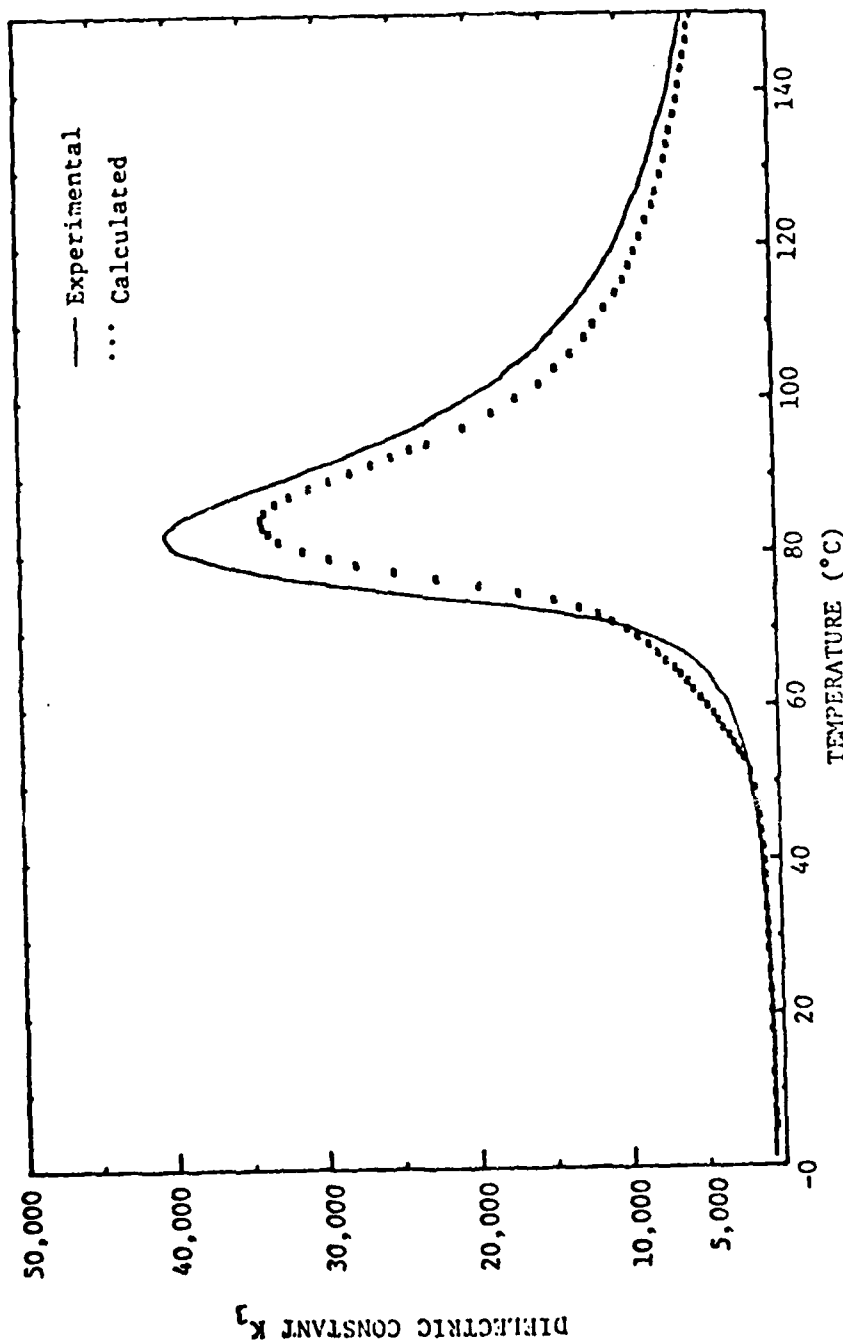
Fig. 7. The measured dielectric constant K_3 compared to the calculated using the distributed LGD model.

14
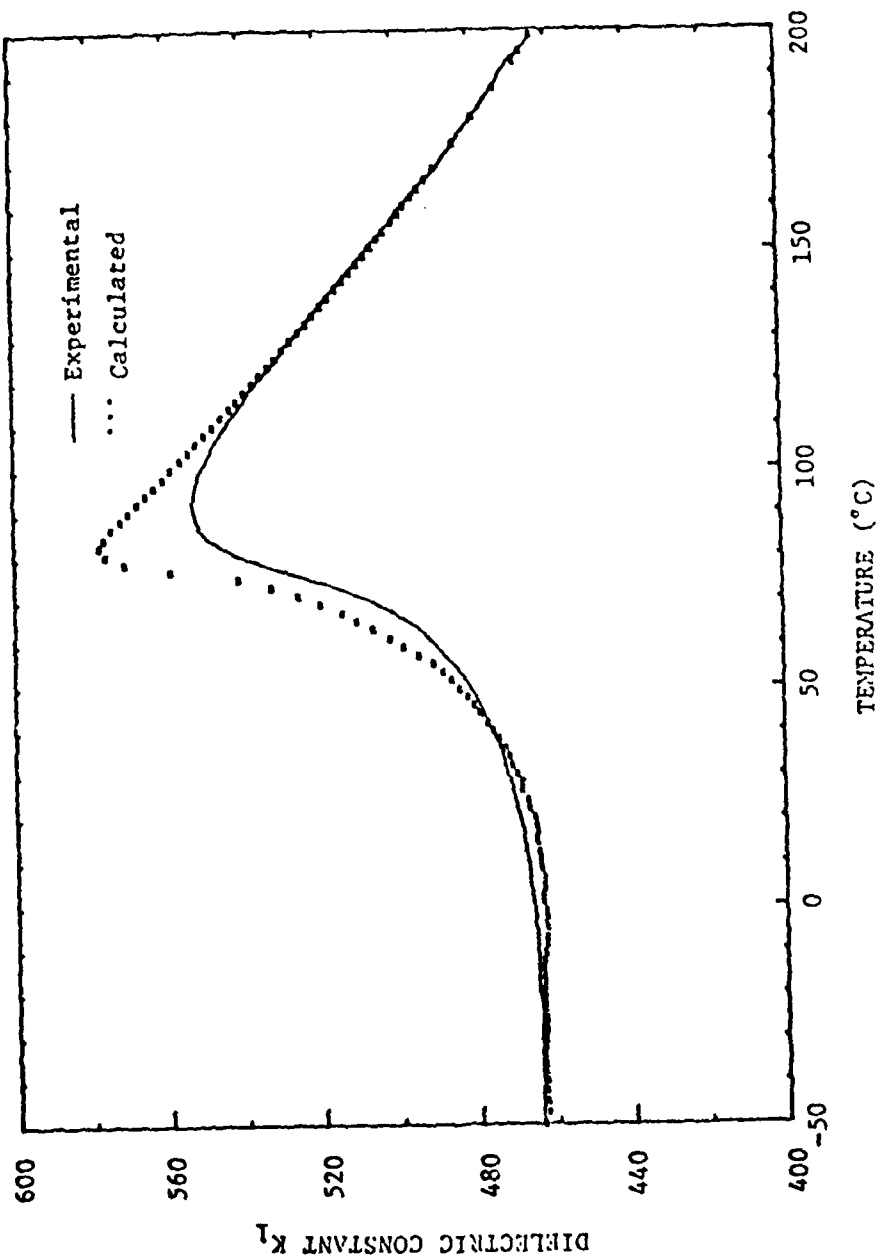
MRDC41007.18AR

Fig. 8. The measured dielectric constant K_1 compared to the calculated using the distributed LGD model.
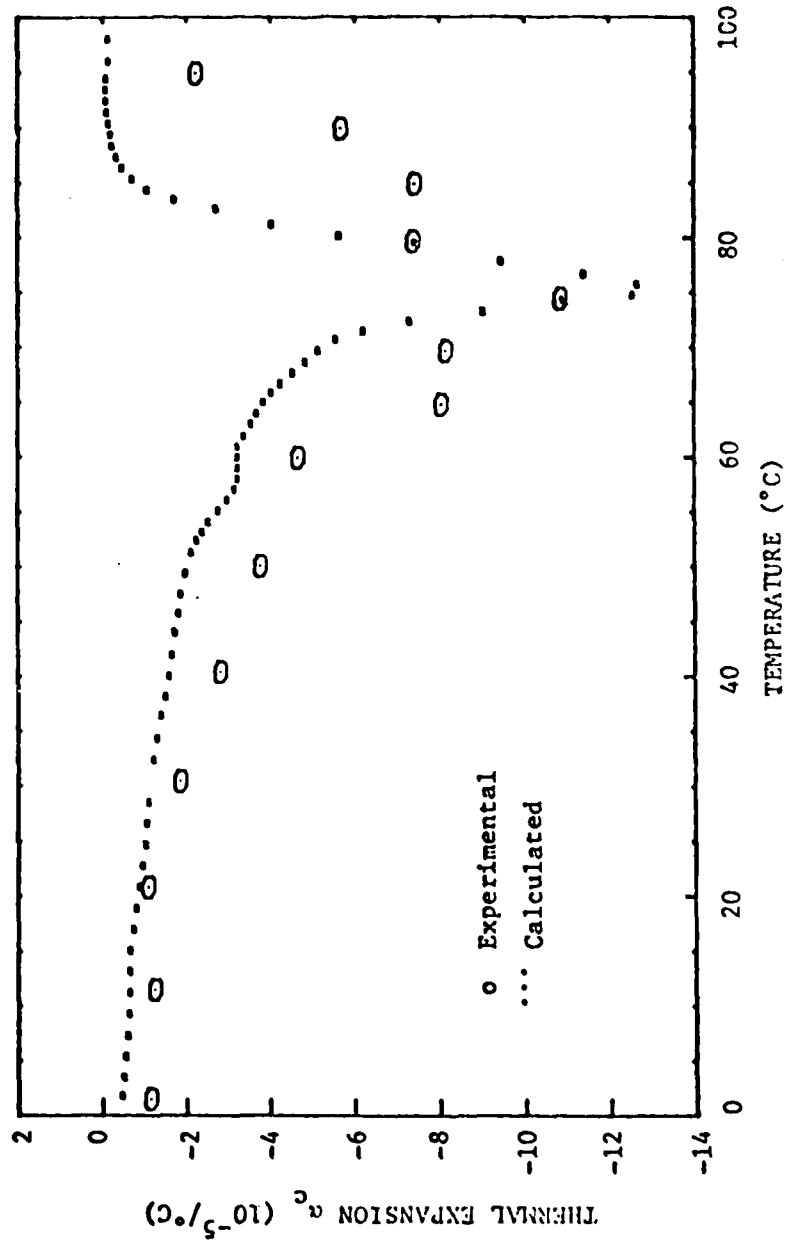
MRDC41007.18AR

Fig. 9. Measured and derived thermal expansion, α_c.
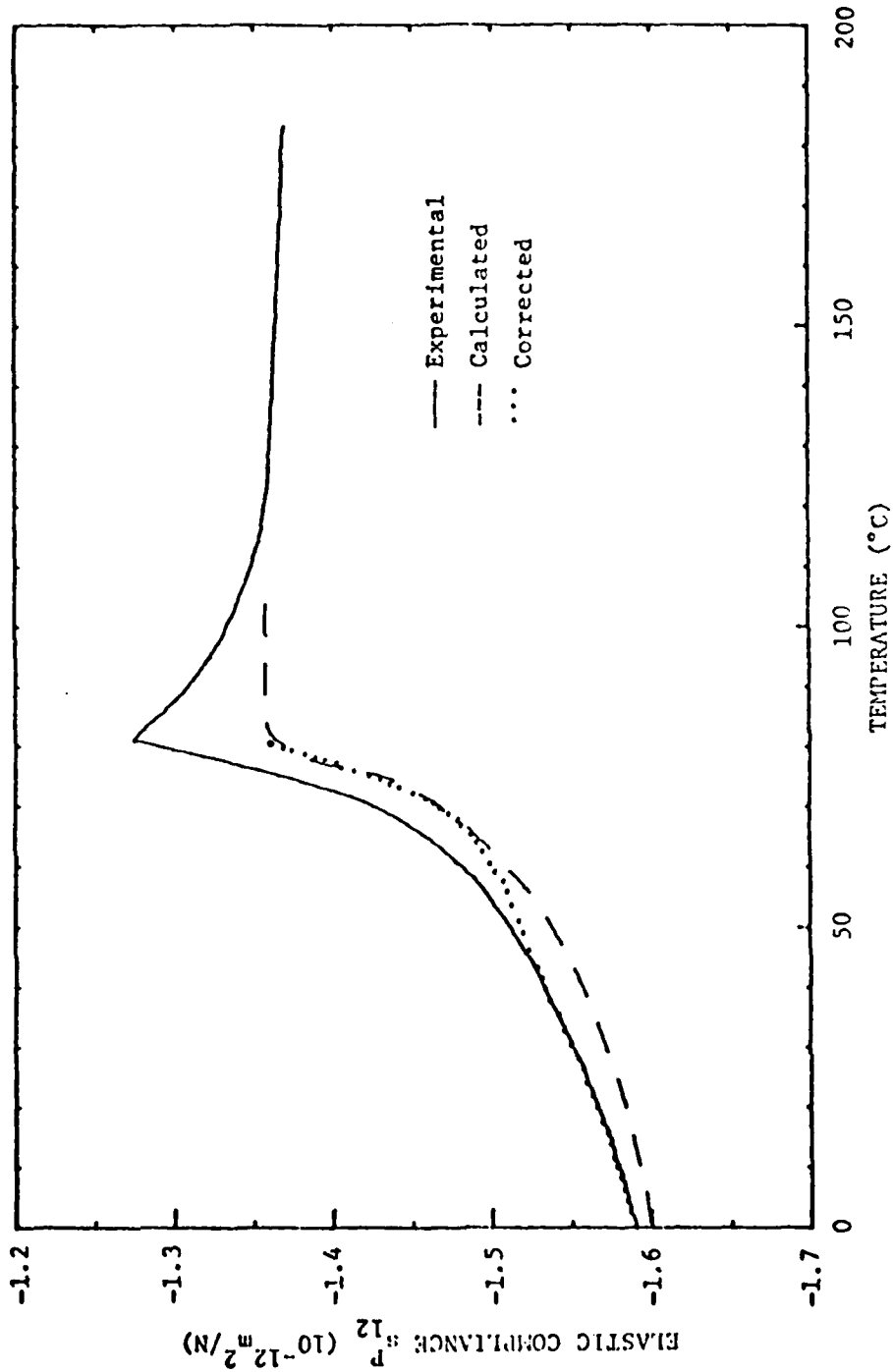
MRDC41007.18AR

Fig. 10. Elastic compliance s_{12}^P measured from piezoelectric resonance data compared to s_{12} derived using R_{312} value determined in paralelectric phase.

17
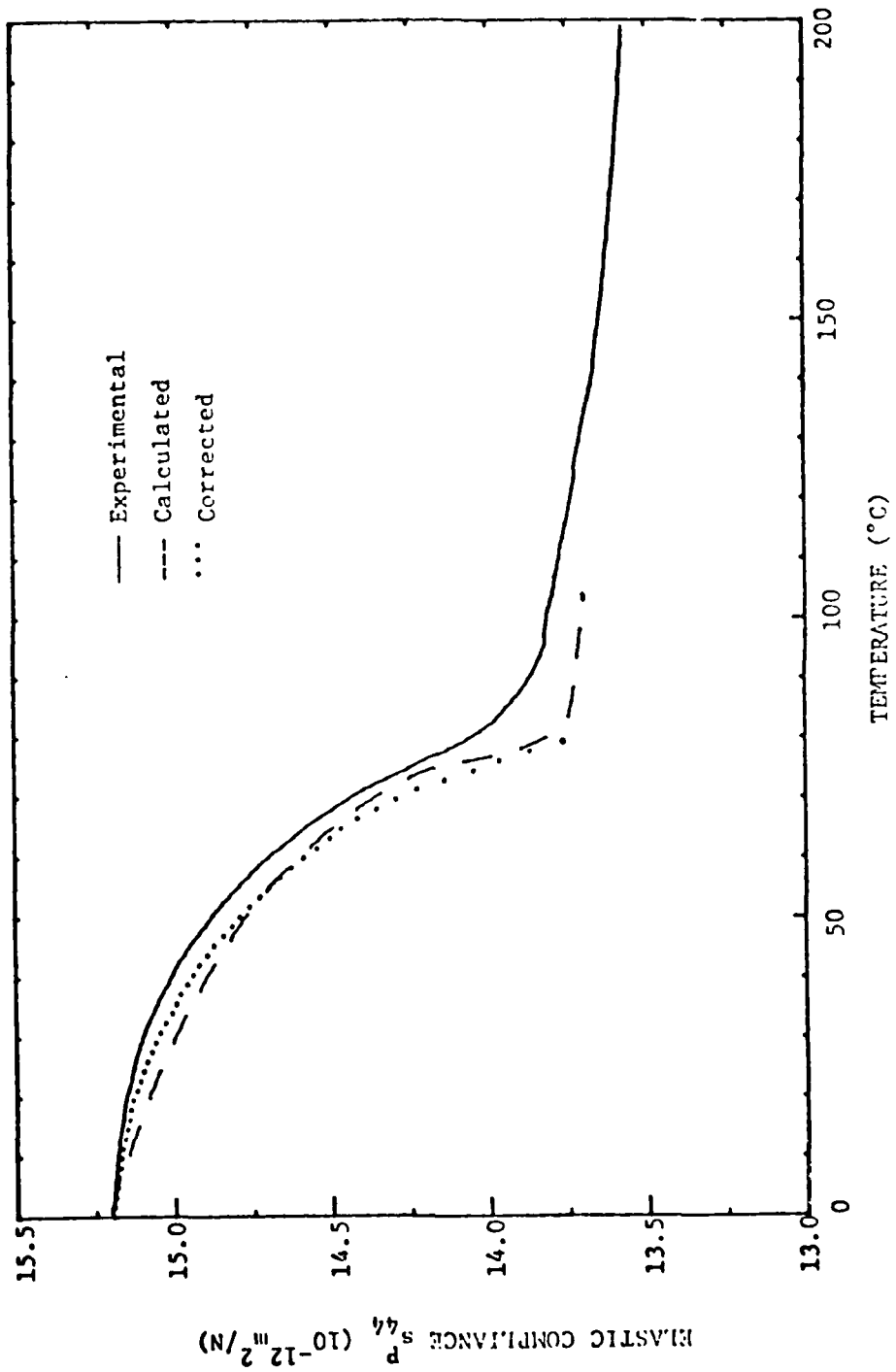
Fig. 11. Elastic compliance s_{44}^P measured from piezoelectric resonance data compared to s_{44} derived using n_{344} value determined in piezoelectric phase.

TEMPERATURE (°C)

ELASTIC COMPLIANCE s_{44}^P ($10^{-12} m^2/N$)

TABLE 3

Experimental and Calculated Temperature Coefficients
of Elastic Compliances of SBN 61:39 at Room Temperature

		Experimental	Calculated
Elastic Compliances	s_{11}^P	$+1.2 \times 10^{-4}/°C$	$+1.8 \times 10^{-4}/°C$
	s_{12}^P	-9.2	-8.3
	s_{13}^P	$+0.63$	-9.7
	s_{33}^P	$+5.0$	-15
	s_{44}^P	-2.3	-4.5
	s_{66}^P	$+0.8$	$+0.9$

tric constant. This is not adequately described by the static phenomenology and is probably due to the large thermal fluctuations in P_3^2 which occur for temperatures in this region. Nonetheless, the phenomenological method does appear to offer the best avenue for predicting the properties which is presently available.

Comparison with the very limited data available for other tetragonal bronze ferroelectric compositions suggests that:

1. The $\alpha_{ijk}\ldots$ stiffness parameters of the thermodynamic function do <u>not</u> change markedly with cation makeup, and that the ferroelectric properties are dominated by the composition dependence of the Curie temperatures Θ_1 and Θ_3.

2. The lower order elasto:dielectric coupling constants Q_{31}, Q_{33} and Q_{44} also do not appear to change markedly across a wide range of bronze compositions.

It thus becomes of cardinal importance to demonstrate for at least two more tetragonal bronzes of widely different cation makeup that the Φ_{3ij} constants themselves do not change markedly with composition.

At that point, it will then be possible to manipulate the LGD equations with some confidence to derive the whole family of properties which are potentially available. By keying the parameters Θ_1, Θ_3 and the Curie range $\Delta\Theta$ to the cation makeup, it should then be possible to select optimum compositions for specific elastic wave device functions. As an example, we calculate (Figs 12 and 13) the effect on the permittivity K_{11} and the piezoelectric constant d_{15} of increasing Θ_1, in the SBN 61:39 bronze without modifying the other thermodynamic parameters. It may be noted that d_{15} increases markedly as Θ_1 increases, giving a possible mechanism for enhancing the coupling coefficient to very high levels.

When the validity and consistency of the LGD approach have been completely tested on the tetragonal bronze crystals, we must turn our attention to the alternative family of orthorhomic bronzes whose elastic properties will be markedly influenced by the Φ_{ijk} parameters.
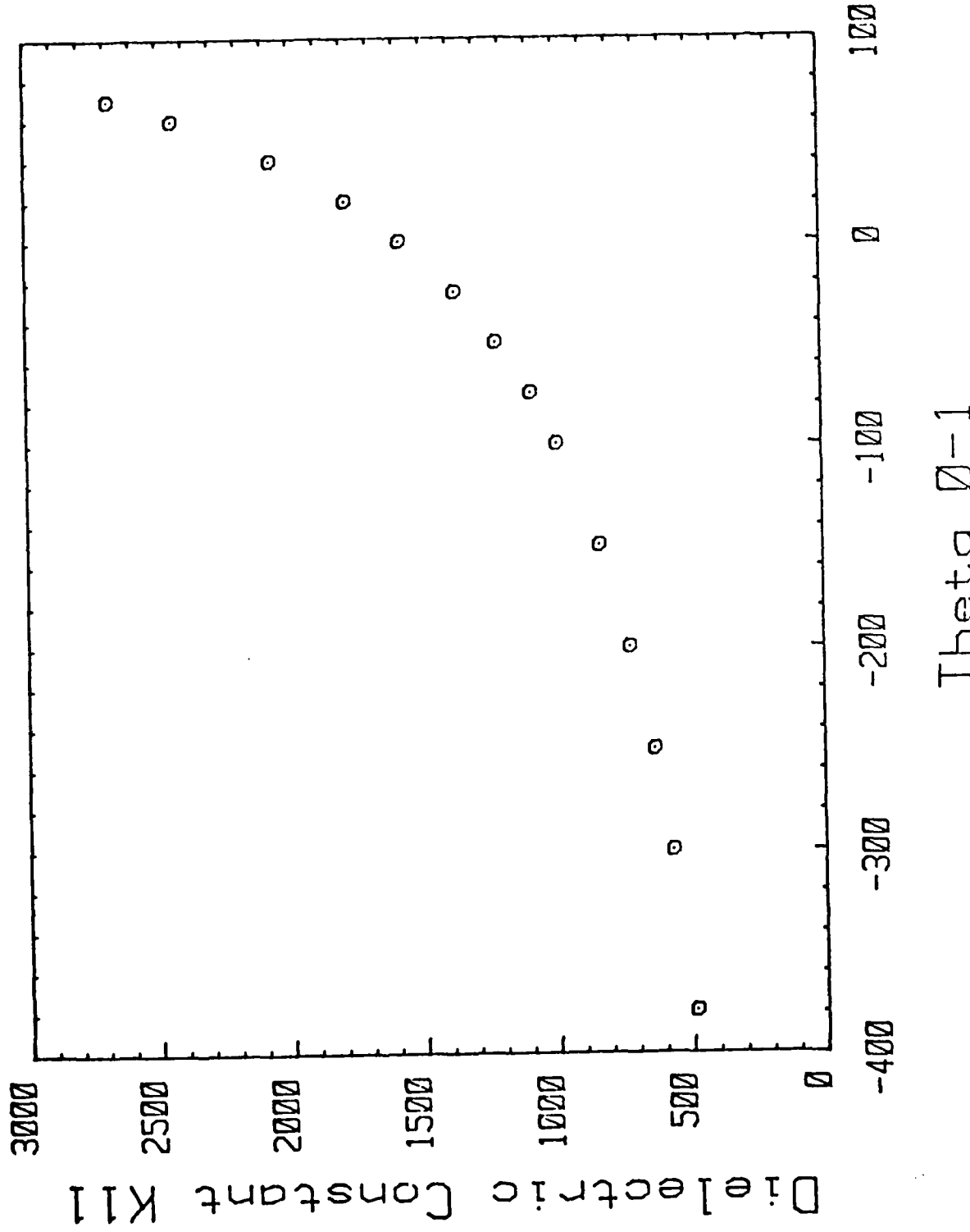
MRDC41007.18AR

Fig. 12. Calculated dielectric permittivity K_{11} as a function of transverse curie temperature Θ_1 in SBN 61:39.
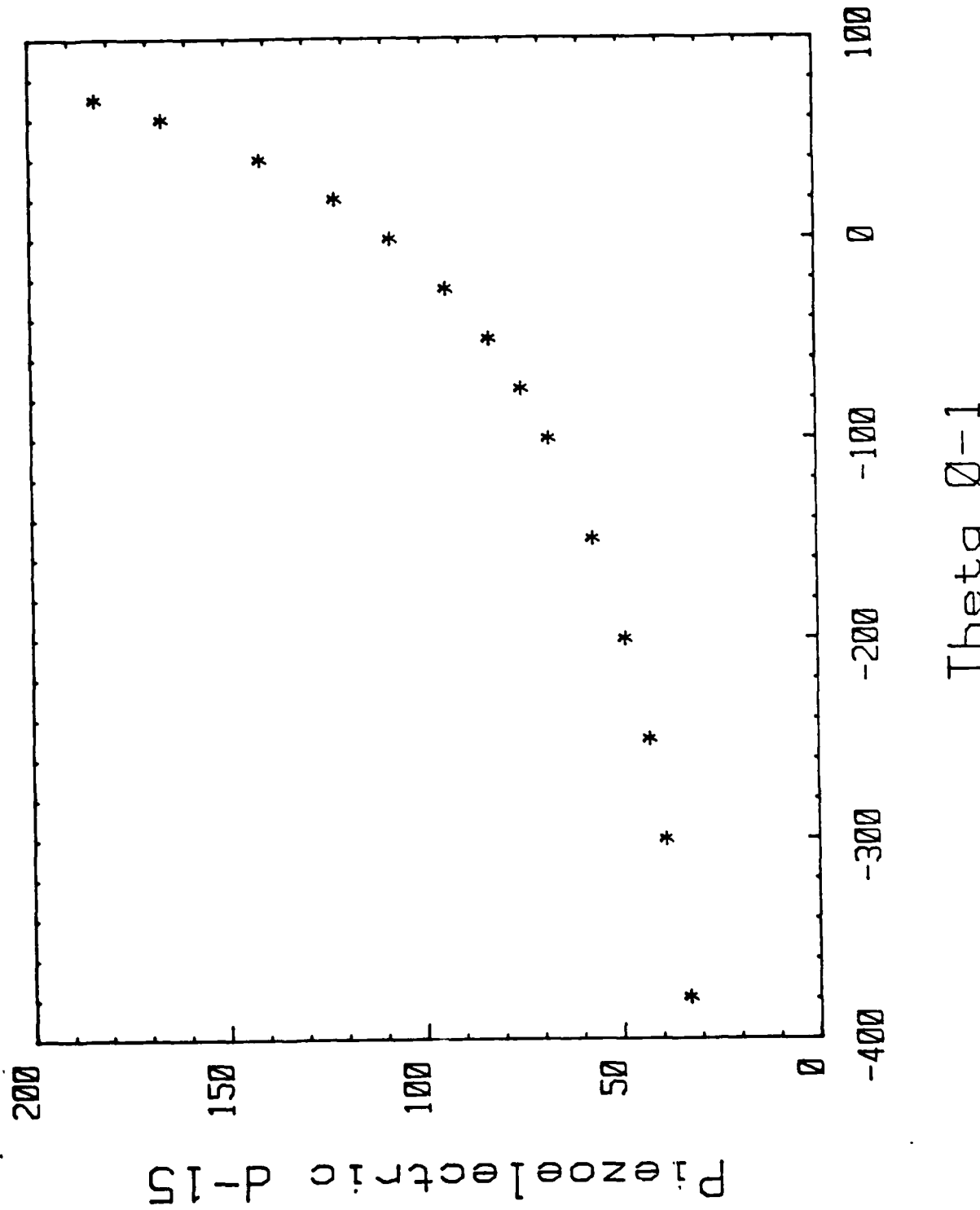
MRDC41007.18AR

Fig. 13. Calculated piezoelectric constant d_{15} as a function of transverse curie temperature Θ_1 in SBN 61:39.

In these bronze families, it will be important to repeat the full experimentation carried out here for the tetragonal compositions. If again the independence from cation makeup can be proven, the previous method can now be applied to all presently known bronze family crystals.

It should be stressed that while the present work is focused upon the elastic response, as a secondary consequence of the thermodynamic method, we are building up a powerful correlation of all nonlinear elasto-dielectric properties which will be of major help for all types of applications using the simple ferroelectric bronzes.

The work described and discussed here has been presented more fully in the Ph.D. thesis by Thomas R. Shrout, "A Phenomenological Theory for Predicting the Temperature Dependence of Elastic Compliance in Simple Proper Ferroelectric Tungsten Bronzes," The Pennsylvania State University (1981). This work was judged to be the outstanding thesis in materials studies in Penn State for 1981 and was recipient of the Xerox Award.

More summarized accounts have been presented at the 34th Annual Frequency Control Symposium (25-33, 1980) and at the IEEE Ultrasonics Symposium (414-419, 1980). These papers are included as technical appendices to this report.

3.0 SURFACE ACOUSTIC WAVE (SAW) PROPERTIES

3.1 Theoretical Calculations of Velocity and Coupling

Consider a surface wave propagation along the x_1-axis of a semi-infinite half space with the x_3 axis normal to the surface. The stress equation is given as:

$$\frac{\partial T_{ij}}{\partial x_j} = \rho \frac{\partial^2 U_i}{\partial t^2} \tag{1}$$

where T_{ij} is the stress, U_j the mechanical displacement and ρ the density. The gradient of electric displacement, D_i, for an insulating material such as SBN:61 is zero:

$$\frac{\partial D_i}{\partial x_i} = 0. \tag{2}$$

For piezoelectric material, the equations of state are given as:

$$T_{ij} = C_{ijkl}^E S_{kl} - e_{kij} E_k \tag{3}$$

$$D_i = e_{ikl} S_{kl} + \epsilon_{ik}^S E_k \tag{4}$$

where $S_{kl} = \frac{1}{2}(\partial U_k/\partial x_1 + \partial U_1/\partial x_k)$ are components of strain, $E_k = -\partial\phi/\partial x_k$ the electric field, C_{ijkl} the elastic constants at constant electric field, e_{kij} the piezoelectric constants and ϵ_{ik}^S the dielectric permittivity tensor at constant strain.

Substituting Eqs. (1) and (2) into (3) and (4) gives

$$\frac{\partial T_{ij}}{\partial x_j} = \frac{1}{2} C_{ijkl}^E \frac{\partial}{\partial k_j}\left(\frac{\partial U_k}{\partial k_1} + \frac{\partial U_1}{\partial x_k}\right) + e_{kij} \frac{\partial^2\phi}{\partial x_j \partial x_k} = \rho \frac{\partial^2 U_i}{\partial t^2} \tag{5}$$

$$\frac{1}{2} e_{ikl} \frac{\partial}{\partial x_i}\left(\frac{\partial U_k}{\partial x_1} + \frac{\partial U_1}{\partial x_k}\right) - \epsilon_{kl}^S \frac{\partial^2\phi}{\partial x_i \partial x_k} = 0 \tag{6}$$

24

i, j, k, l, = 1, 2, 3

Assuming a particle displacement of the form

$$U_j = \alpha_j e^{ikbx_3} e^{ik(x_1 - vt)} \qquad (7)$$

where α_j are unit vectors along x_j respectively, wave member $k = 2\pi/\lambda$; b the decay constant with depth, v the phase velocity; and the electric potential as

$$\phi = \alpha_4 e^{ikbx_3} e^{ik(x_1 - vt)} . \qquad (8)$$

Substituting Eqs. (7) and (8) into (5) and (6) gives

$$\begin{pmatrix} \Gamma_{11} - \rho V^2 & \Gamma_{12} & \Gamma_{13} & \Gamma_{14} \\ \Gamma_{12} & \Gamma_{22} - \rho V^2 & \Gamma_{23} & \Gamma_{24} \\ \Gamma_{13} & \Gamma_{23} & \Gamma_{33} - \rho V^2 & \Gamma_{34} \\ \Gamma_{14} & \Gamma_{24} & \Gamma_{34} & \Gamma_{44} \end{pmatrix} \cdot \begin{pmatrix} \alpha_1 \\ \alpha_2 \\ \alpha_3 \\ \alpha_4 \end{pmatrix} = 0 \qquad (9)$$

where

$$\Gamma_{11} = C_{55}b^2 + 2C_{15}b + C_{11}$$
$$\Gamma_{22} = C_{44}b^2 + 2C_{46}b + C_{66}$$
$$\Gamma_{33} = C_{33}b^2 + 2C_{35}b + C_{55}$$
$$\Gamma_{12} = C_{45}b^2 + (C_{14} + C_{56})b + C_{16}$$
$$\Gamma_{13} = C_{35}b^2 + (C_{13} + C_{55})b + C_{15}$$
$$\Gamma_{23} = C_{34}b^2 + (C_{36} + C_{45})b + C_{56}$$
$$\Gamma_{14} = e_{35}b^2 + (e_{15} + e_{31})b + e_{11}$$
$$\Gamma_{24} = e_{34}b^2 + (e_{14} + e_{36})b + e_{16}$$
$$\Gamma_{34} = e_{33}b^2 + (e_{13} + e_{35})b + e_{15}$$

with the electric term

$$\Gamma_{44} = -(\epsilon_{33}b^2 + 2\epsilon_{13}b + \epsilon_{11}).$$

The secular Eq. (9) is applied to the piezoelectric material and the matrix of coefficients is reduced to a polynomial in b. In the completely general case, the polynomial is of 8th order and 8 complex roots, b_j, are solved for. However, *only those roots which cause decay to zero with decreasing* x_3 are retained. This results in four solutions to the equation of motion.

The total solution to the boundary-value problem is taken as a sum of the four partial solutions,

$$\bar{u}_j = \sum_{n=1}^{4} C_n \alpha_j^{(n)} e^{ikb_n x_3} e^{ik(x_1 - vt)} \qquad j = 1,2,3 \qquad (10)$$

$$\bar{\phi} = \sum_{n=1}^{4} C_n \alpha_4^{(n)} e^{ikb_n x_3} e^{ik(x_1 - vt)}$$

These summation solutions are substituted into the appropriate boundary conditions at the free surface,

    1.   Vanishing of sagittal shear stress at the free surface,
        $T_{31}(x_3=0) = 0$

    2.   Vanishing of vertical compressional stress at the free surface,
        $T_{33}(x_3=0) = 0$

    3.   Vanishing of transverse shear stress at the free surface,
        $T_{32}(x_3=0) = 0$

    4.   Continuity of normal component of electric displacement at the free surface,
        $D_3(x_3=0) = kE_0\phi(x_3=0).$

If the surface is conducting, the the condition of displacement current is *changed to reflect a zero potential at the surface.* Thus the four boundary conditions provide four equations in the four unknowns, C_n. In order to obtain

non-trivial solutions to this set of homogeneous equations, a 4x4 determinant, successive values of v are chosen until the boundary condition determinant is equal to zero.

A computer program based upon the above analysis was developed to theoretically predict SAW velocity and coupling on SBN. For this analysis, the following piezoelastic constants were used:

$$c_{11}^{E} = 2.47 \times 10^{11} \qquad e_{31} = -0.555$$

$$c_{12}^{E} = 0.991 \qquad e_{33} = 12.624$$

$$c_{13}^{E} = 0.756 \qquad e_{15} = 0\ 5$$

$$c_{1?}^{E} = 0.646$$

$$c_{66}^{E} = 0.694 \qquad \epsilon_{11}^{S}/\epsilon_{0} = 462$$

$$\rho = 5.3 \times 10^{3} \qquad \epsilon_{33}^{S}/\epsilon_{0} = 633$$

The constant e_{15} as determined by bulk resonator measurements was somewhere in the range 2 to 10; however, because of spurious modes in X-cut thickness shear plates, the actual value could not be determined with any accuracy. Fortunately, SAW transducers fabricated on Z-cut, X propagating substrates are practically independent of e_{31} and e_{33}. Hence, a measure of surface wave coupling on Z-cut SBN:61 provides an indirect measure of e_{15}. In order to determine the proper value, shorted and open circuit velocity was calculated for Z-cut, X propagation surface waves. The results are shown in Fig. 14. The experimentally measured value of k^2 was 0.018, hence the correct value of $\Delta V/V$ is 0.009. From Fig. 14, this corresponds to a value of e_{15} of 4.0.

Using the proper value of e_{15}, SAW velocity and $\Delta V/V$ was calculated for the Z-cut, X-cut and (110) cuts along the Z direction as a parameter. The results are shown in Figs. 15-17. Coupling for the Z-cut is essentially constant. Coupling for the X and (110) cuts along the Z direction is approximately equal, 0.0029; however, it is zero for propagation 90° from the Z axis.

27

SAW VELOCITY vs E$_{15}$ (SBN-61)

MRDC41007.18AR

dv/v vs E$_{15}$ (SBN-61)
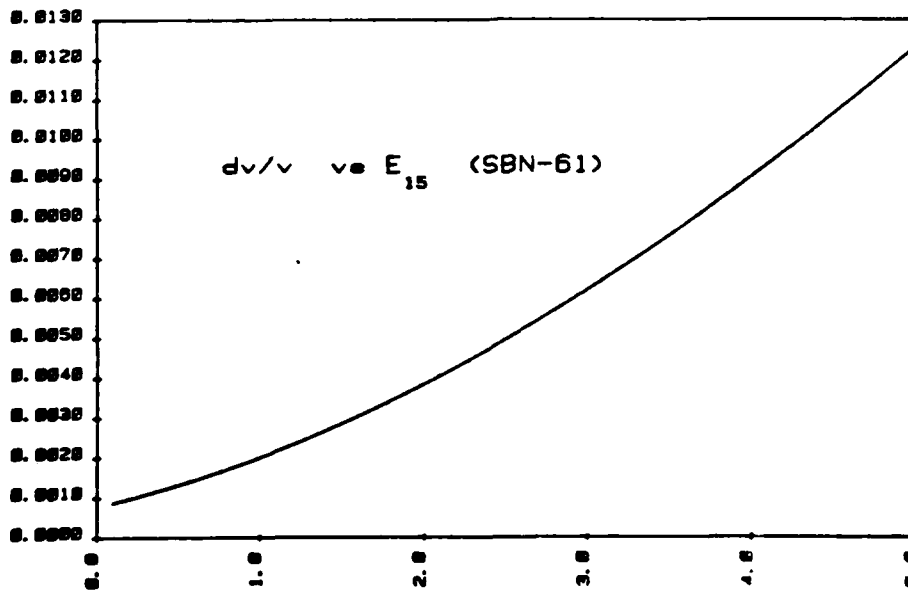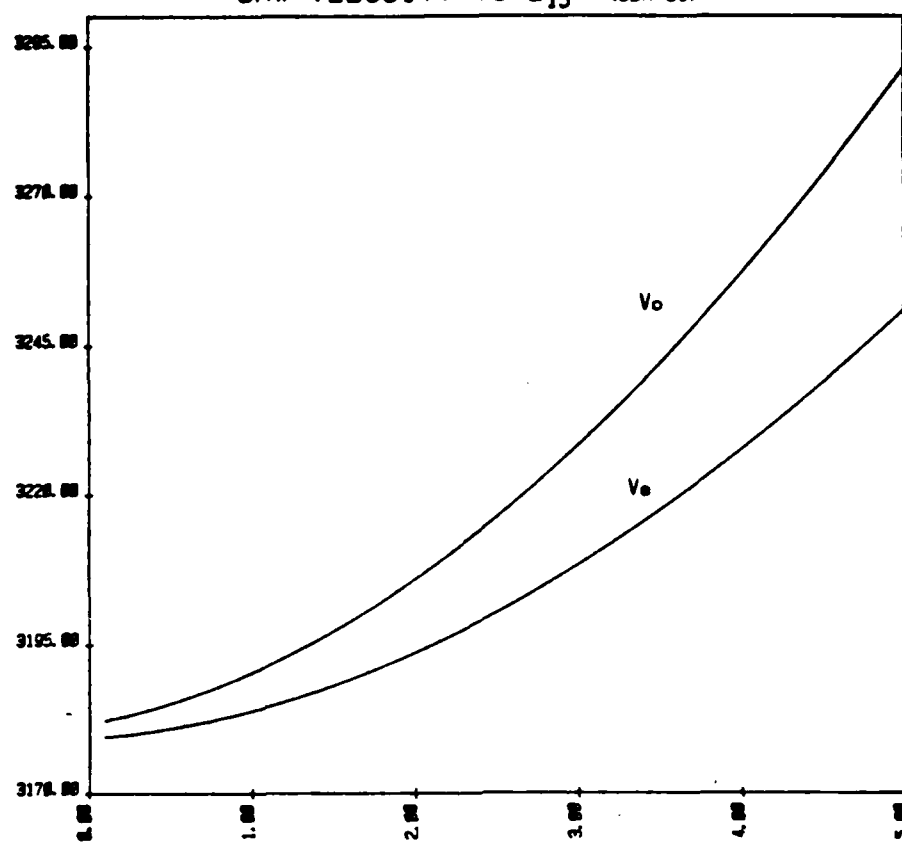
Fig. 14. Theoretical calculations showing the effects of the piezoelectric constant, e$_{15}$, upon surface wave velocity, shorted and unshorted, and the resultant velocity perturbation, $\Delta V/V_o$.

MRDC41007.18AR

SAW VELOCITY   Z-CUT SBN-61
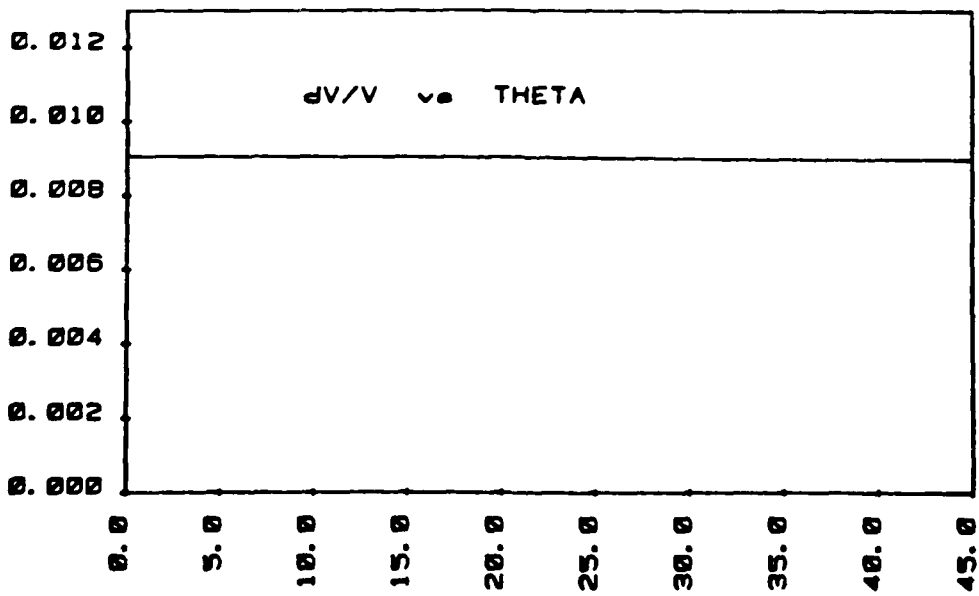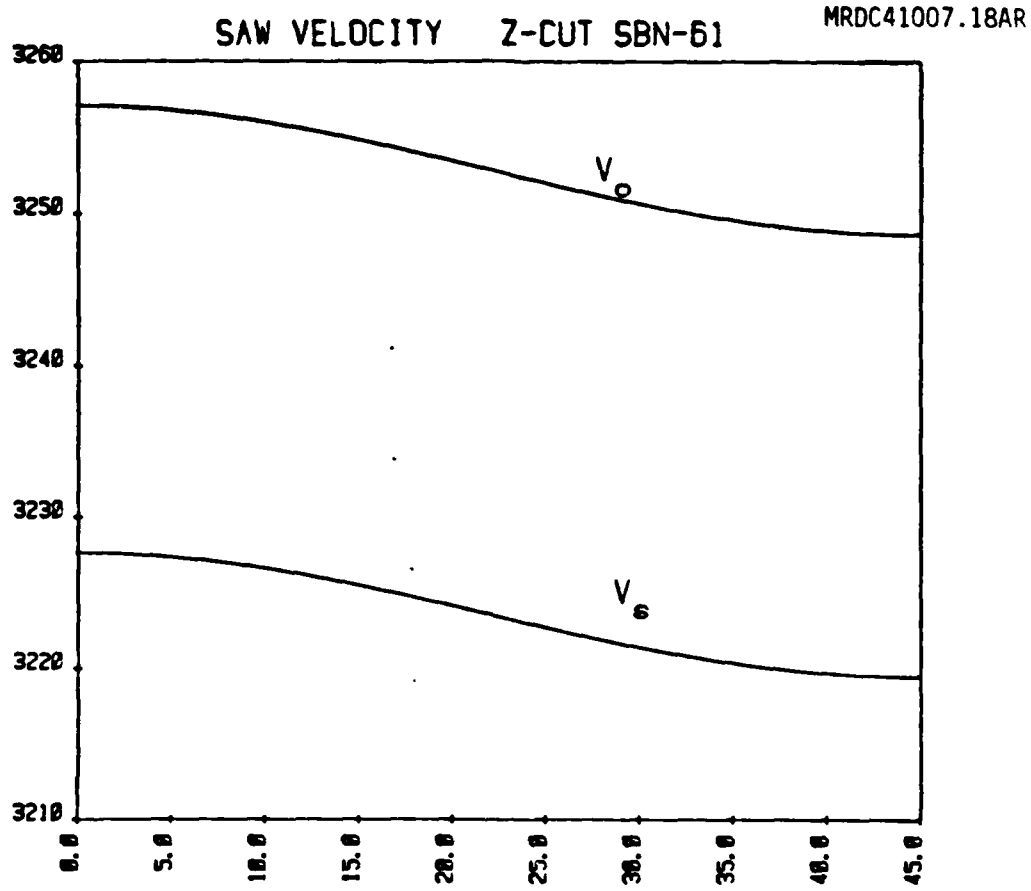
Fig. 15.   SAW velocity and coupling for propagation on Z-cut SBN:61.

29
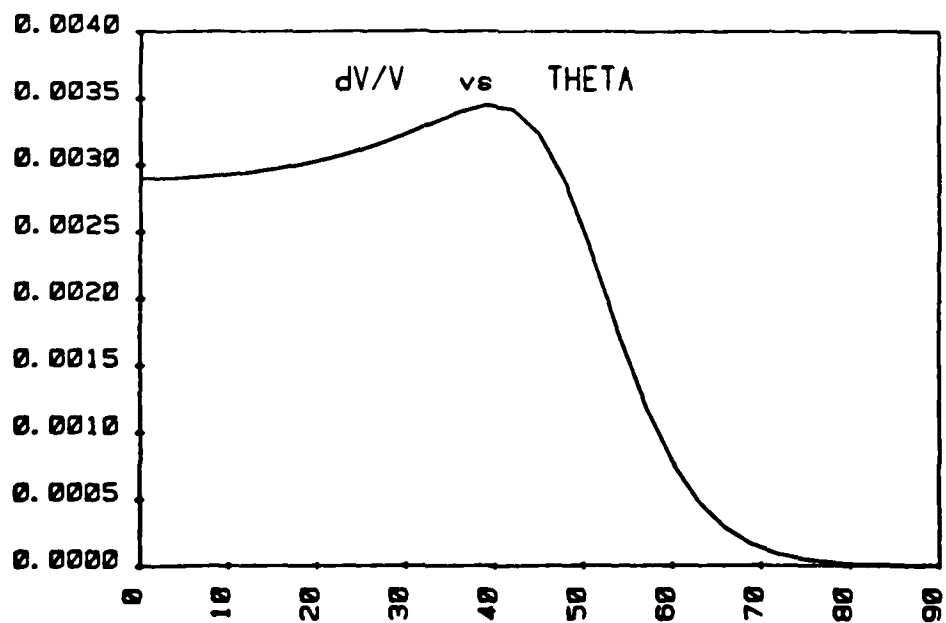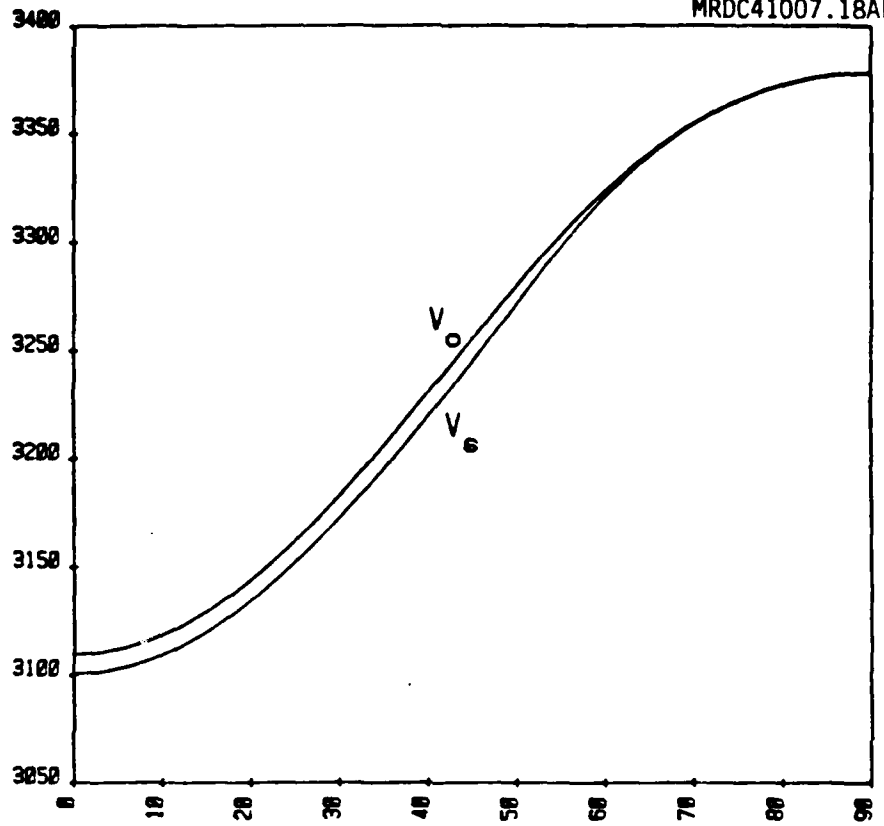
MRDC41007.18AR

Fig. 16. SAW velocity and coupling for propagation on X-cut SBN:61

30
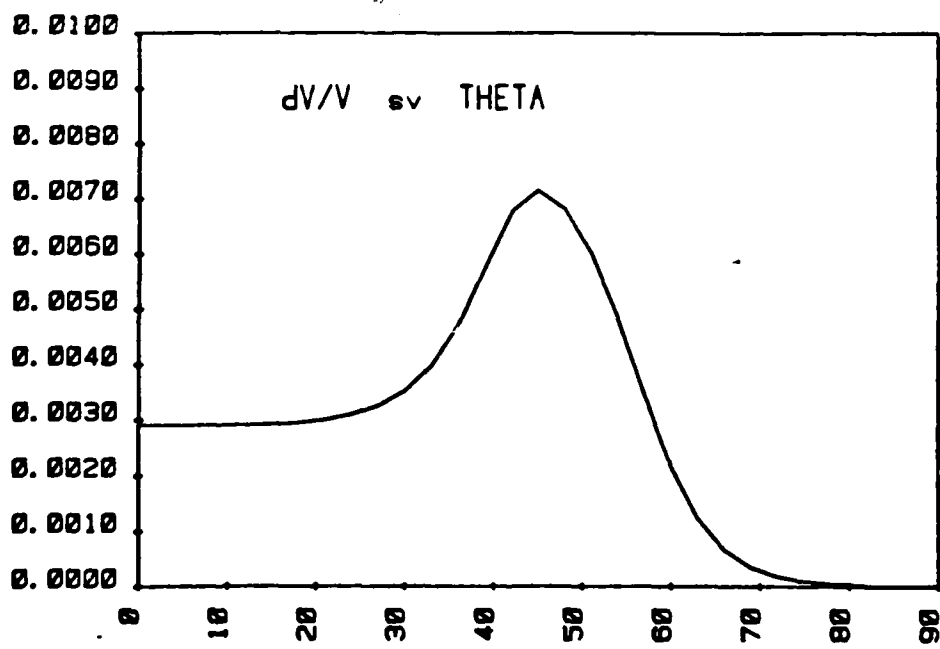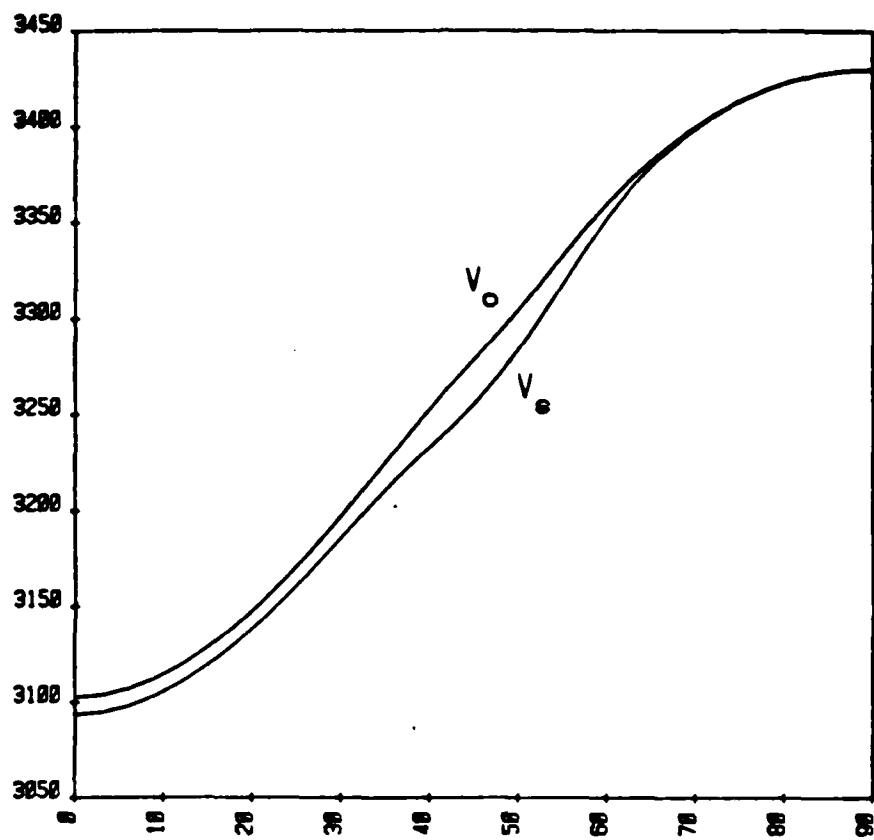
Fig. 17. SAW velocity and coupling for propagation in (110)-cut SBN:61.

MRDC41007.18AR

3.2 Experimental Results

Surface acoustic wave delay lines were fabricated on X-cut, Z-cut and (110)-cut plates of SBN:61. For the X and (110) cuts, propagation was along the Z direction; for the Z-cut, propagation was along the X-axis. Fifteen finger pair transducers were used and the periodicity was 104.4 μm. Transducer electrodes were photolithographically fabricated from aluminum films approximately 1000Å thick using conventional wet etching techniques.

Transducer and delay line characteristics were measured using automatic network analysis and pulse echo techniques. Transducer impedance characteristics were derived from measured scattered parameters with respect to 50 ohm transmission line standards. A new method of transducer modeling was used to determine parameters such as coupling and parasitic reactances. This method used computer generated idt cross-field models coupled with conventional lumped element resistors, inductors, and capacitors for parasitic reactances. The technique was to iteratively perform a multi-valued search to determine the circuit elements which most accurately matched the measured scattering parameters. After determining the best computer fit, the transmission loss through each transducer was calculated and subtracted from the measured delay line insertion loss to yield the loss due to acoustic attenuation. Thus, a measure of acoustic attenuation was also made.

After an initial measurement, the delay line was tested for temperature stability by placing in an oven and varying temperature over a range typically -20°C to +50°C. After temperature cycling and recording amplitude and frequency fluctuations, the transducers were again tested and their equivalent circuit representation determined. The following results were obtained.

3.2.1 Z-Cut, X Propagating

For transducers separated by 0 2 inches, the phase delay was nominally 1.5 μsec and insertion loss was -17.4 dB as shown in Fig. 18. Transducer scattering parameters over the range 20-40 MHz are shown in Fig. 19. The results of a best-fit cross-field model are shown in Fig. 20. The equivalent circuit form and results are shown in Fig. 21(a). After temperature cycling,

MRDC41007.18AR

SBN-61, (001)-X Propagating

(a)

SBN-61, (001)-X Propagating

(b)
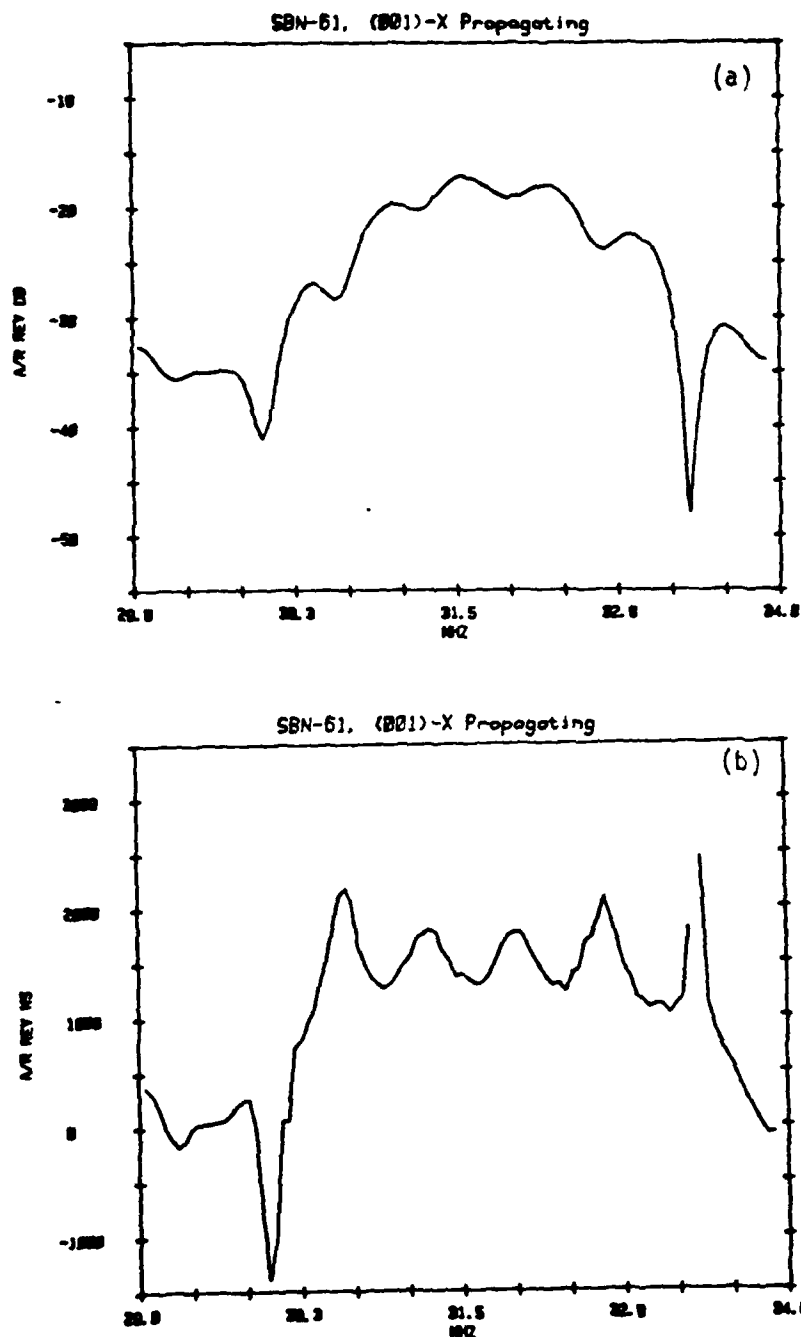
Fig. 18.   Experimental Z-cut, X-propagating delay line response. (a) insertion loss and (b) phase delay.

33

MRDC41007.18AR

SBN-61, (001)-X Propagating

SBN-61, (001)-X Propagating
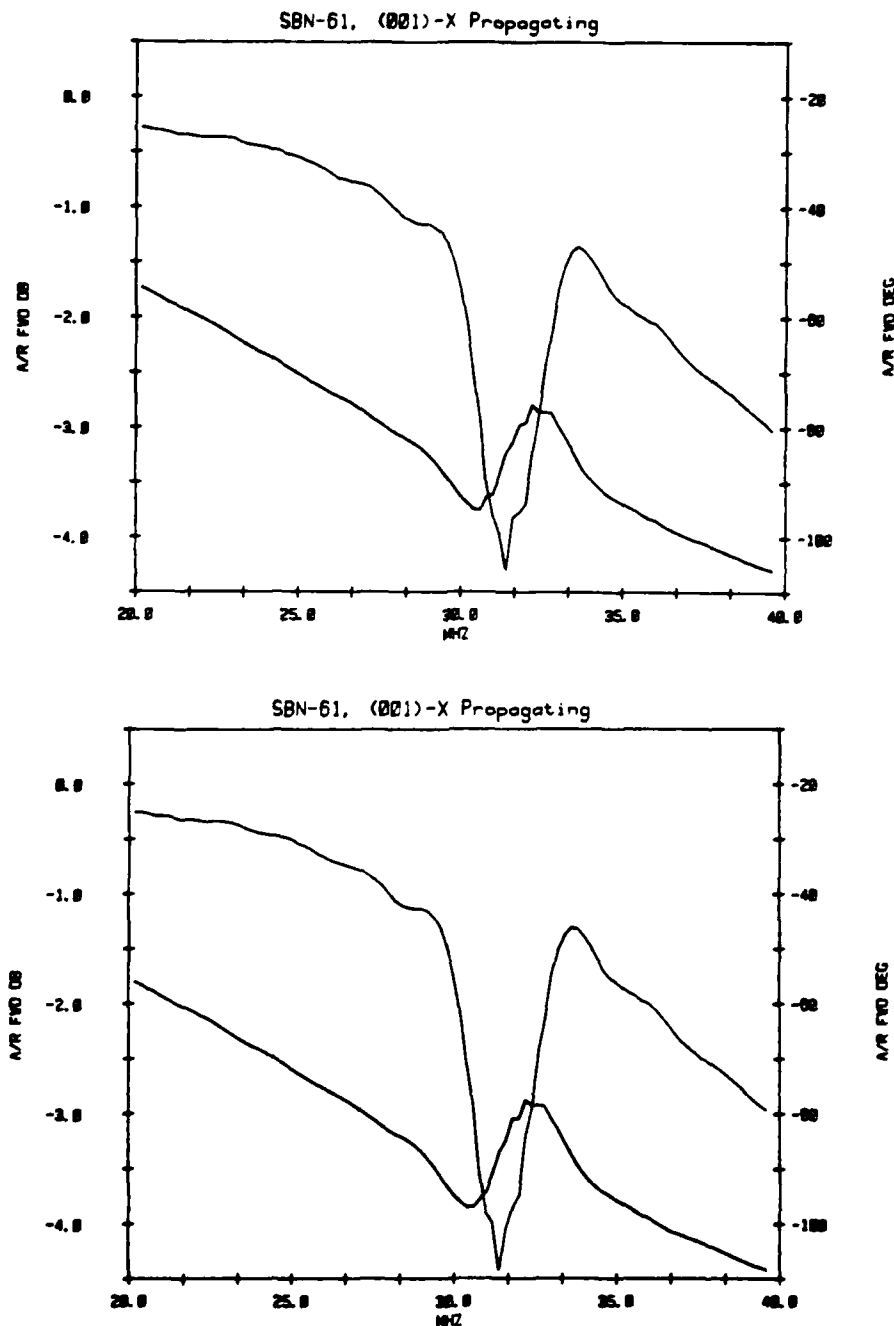
Fig. 19. Experimental Z-cut, X propagating SAW transducer scattering
parameters after poling and before temperature cycling.
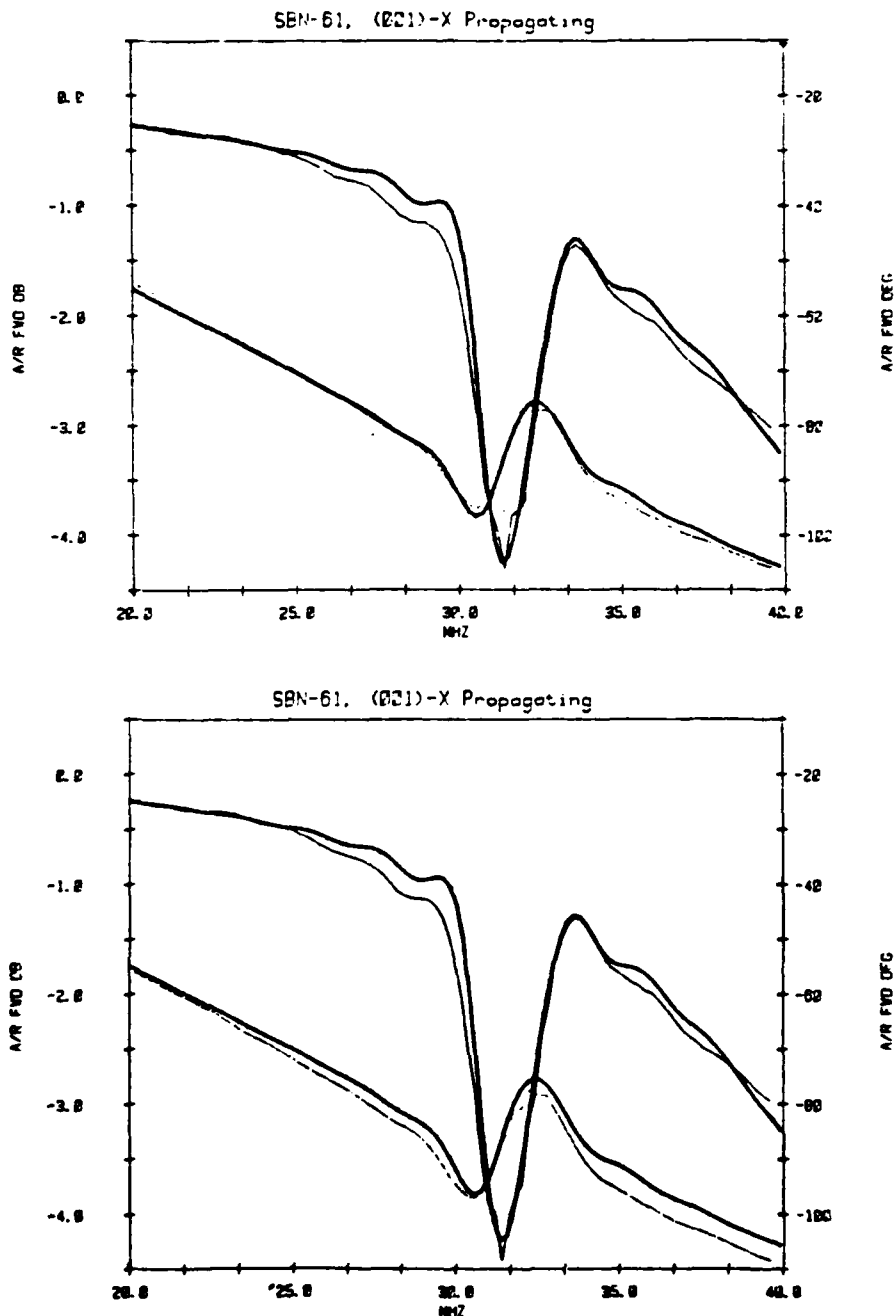
34

Fig. 20.   Comparison between experimental and best fit, crossed-field
computer modeling of transducer scattering parameters.

Z-cut, X propagating SPN-61
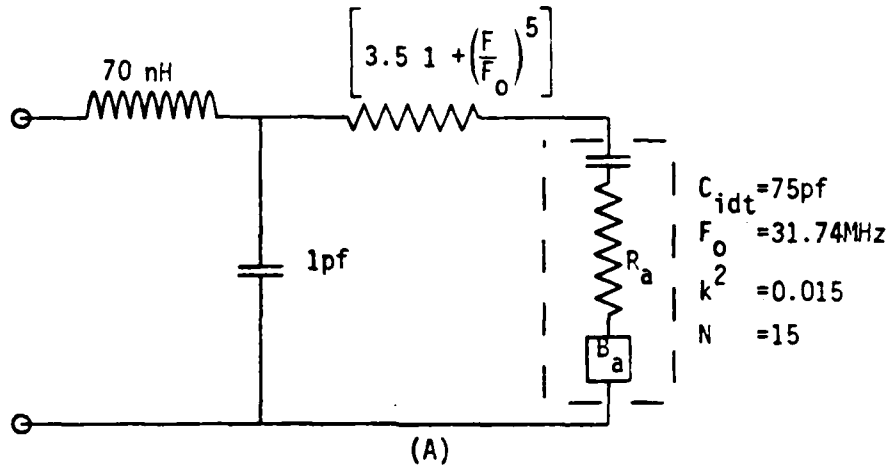
(A)
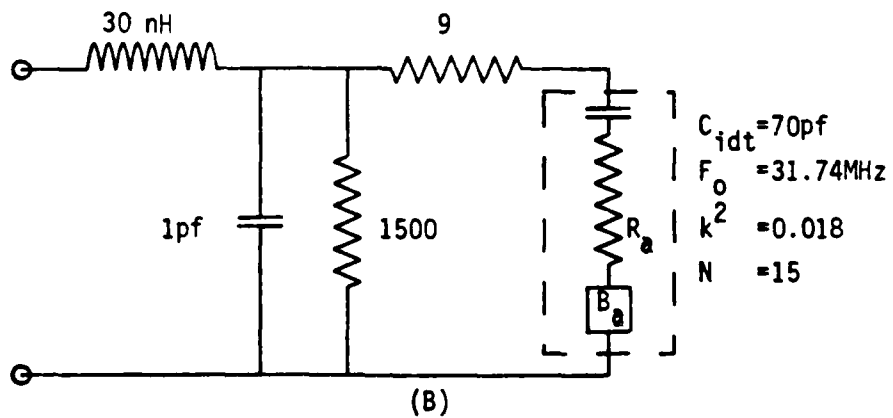
(B)

Fig. 21.   SAW transducer equivalent circuit model (a) before temperature
cycling and (b) after temperature cycling.

36

the transducer scattering parameters are shown in Fig. 22. The best fit cross-field equivalent circuit model is shown in Fig. 21(b). Clearly, temperature cycling the SBN:61 changed the parasitic reactances considerably. Before cycling, the model required frequency dependent resistances to satisfy roll-off in the scattering parameter. After cycling, the frequency dependence was removed; however, the parasitic loss increased. The amount of inductance required is also anomalous. Actual wiring inductance was measured to be less than 15 nH, yet at least 70 nH was initially required to satisfy the phase slope of the transducer scattering parameters. After temperature cycling, the inductance dropped to only 30 nH. Delay line loss calculated from idt S-parameters was -14.7 dB, leaving 2.7 dB loss due to attenuation. Based upon the idt separation, the acoustic attenuation was approximately 5.3 dB/cm at a resonant frequency of 31.9 MHz.

In summary, the coupling coefficient was 0.015-0.018; the SAW velocity approximately 3300 m/sec; the acoustic attenuation was typically 5.3 dB/cm.

3.2.2   X-Cut, Z Propagating

Performing transducer modeling as discussed for Z-cut transducers, the best fit crossed-field model is shown in Fig. 23. The actual comparison between measured and computed scattering parameters is shown in Fig. 24. The measured surface wave velocity based on phase delay and pulse echo measurements was 3193 m/sec. The measured delay line loss was -25.4 dB and the calculated loss based on transducer scattering parameters was -25.0 dB. This yields an acoustic attenuation of 0.8 dB/cm at 30.5 MHz. The piezoelectric coupling for SAW was 0.0055.

3.2.3   (110)-Cut, Z Propagating

The delay line loss was typically 41 dB and phase delay 6.5 μsec for transducers separated by 0.8 inches (2.032 cm). Transducer scattering parameters before temperature cycling are shown in Fig. 25 and after temperature cycling in Fig. 26 along with the best fit cross-field model results. The transducer equivalent circuits for before and after are shown in Fig. 27. In this case, the delay line was substantially longer than previous cases and the effects of propagation path length were increased. Delay line loss calculated
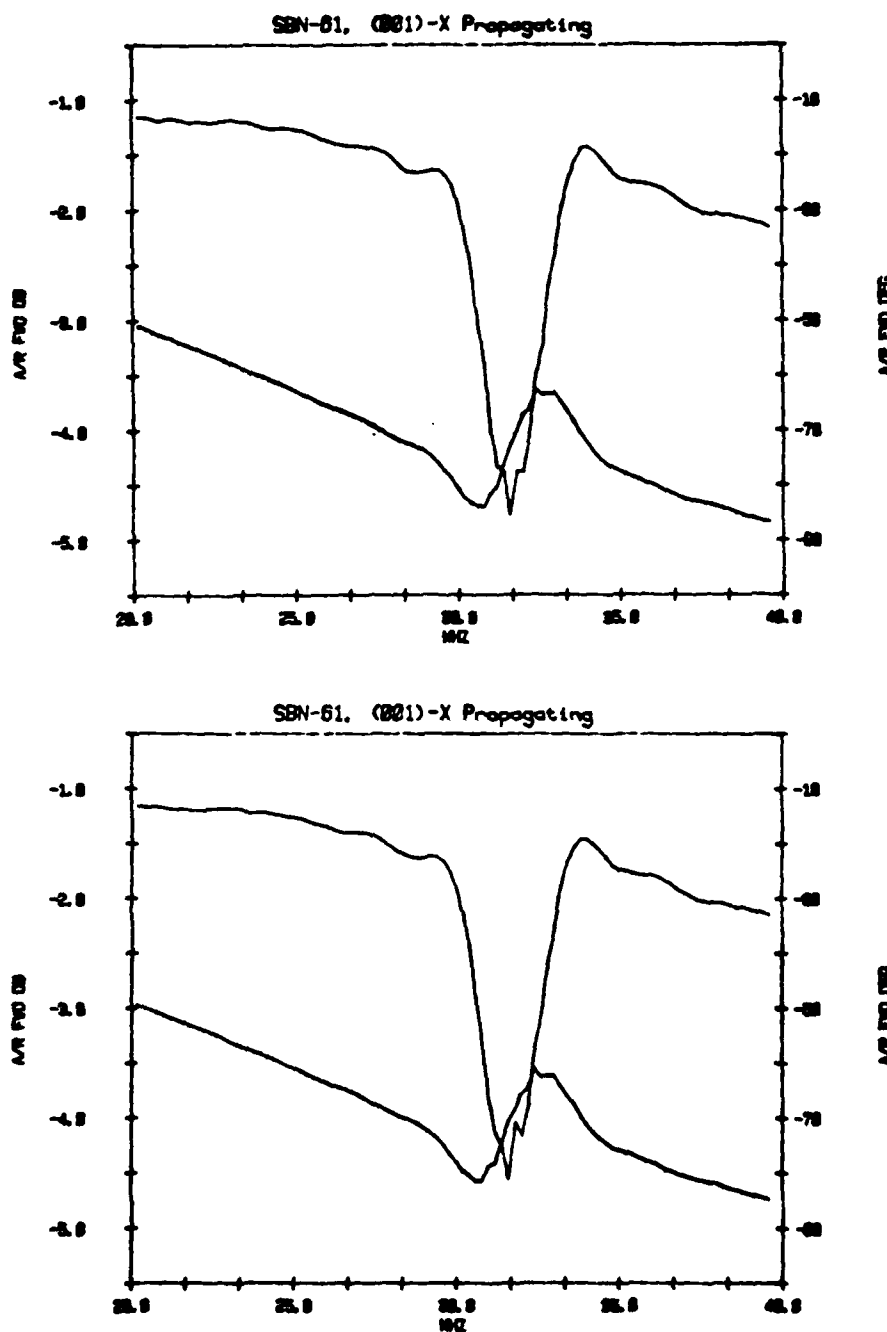
MRDC41007.18AR

Fig. 22. SAW transducer experimental scattering parameters after tempera-
ture cycling Z-cut, X propagating.

$$C_{idt} = 60pf$$
$$F_o = 30.5\ mHz$$
$$k^2 = 0.0055$$
$$N = 15$$
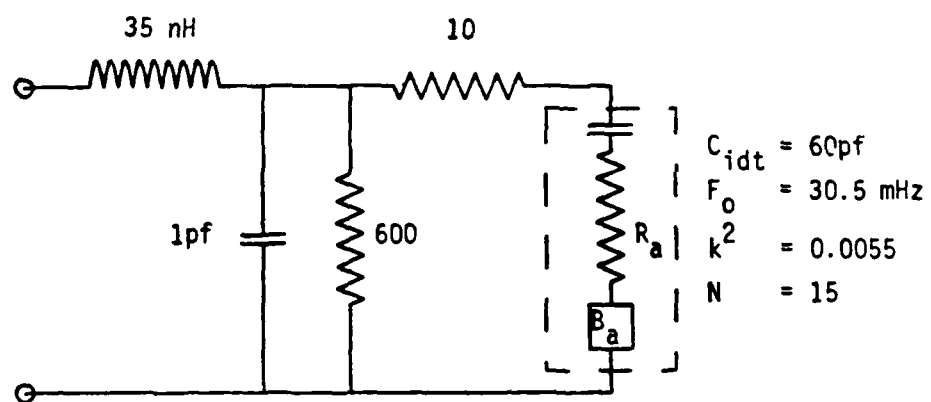
Fig. 23. SAW transducer equivalent circuit model for X-cut, Z propagating transducers.
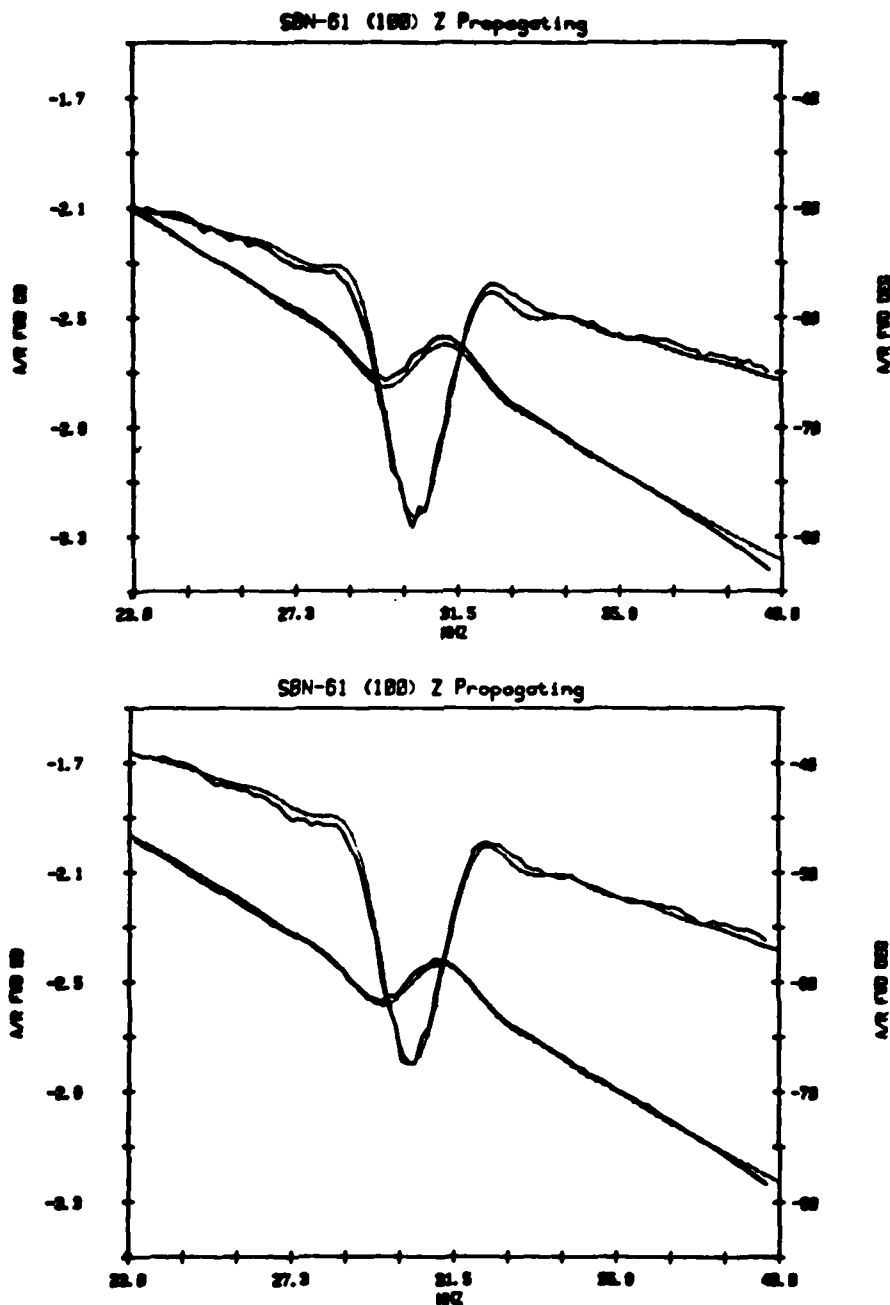
MRDC41007.18AR


Fig. 24. Comparison between experimental and best fit, crossed-field computer modeling of transducer scattering parameters for X-cut, Z propagating.

SBN-61, (110)-Z Propagating

SBN-61, (110)-Z Propagating
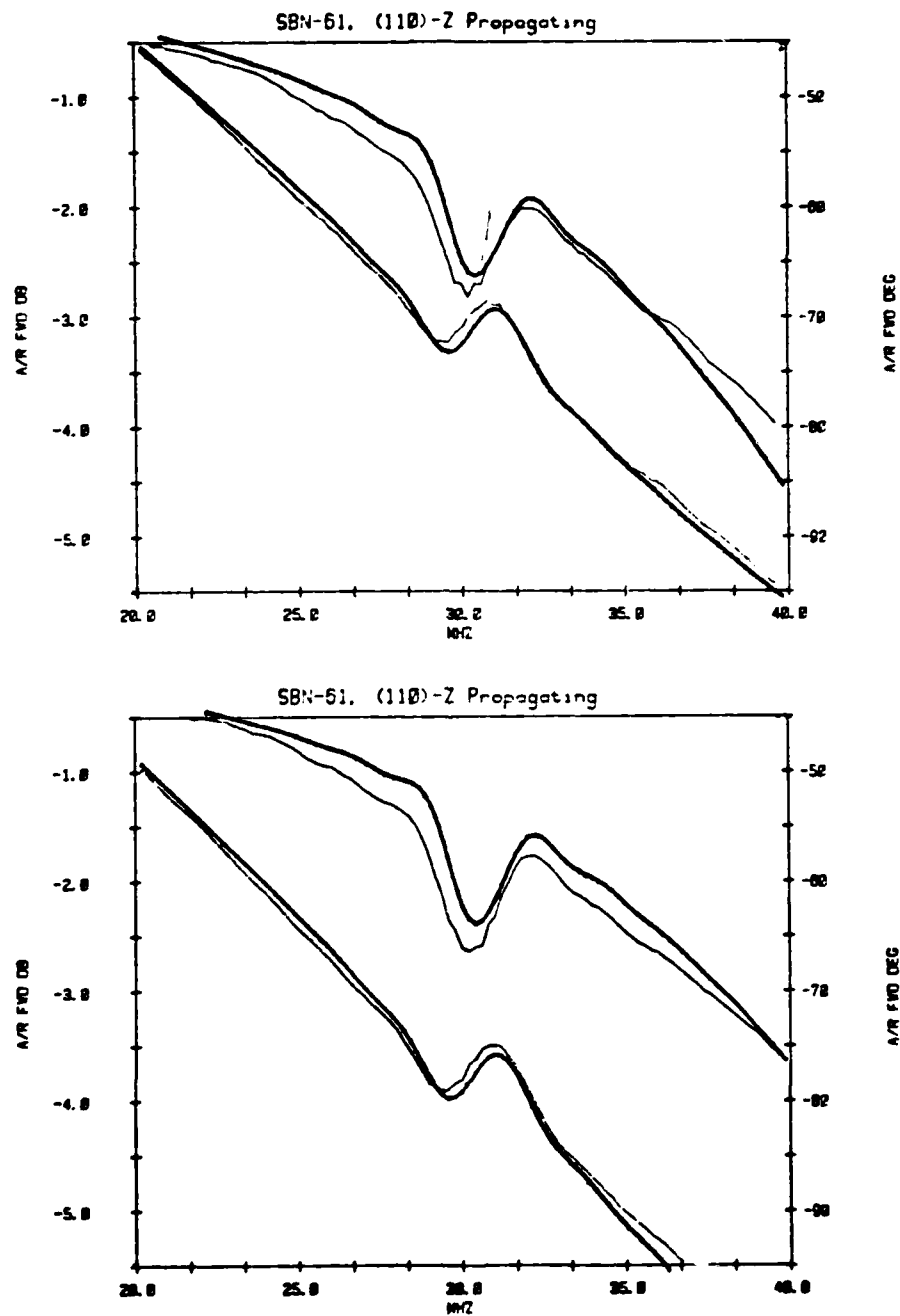
Fig. 25. Comparison between experimental and best fit, crossed-field com-
puter modeling of transducer scattering parameters for (110)-cut,
Z propagating SAW transducers after temperature cycling.

41

SBN-61, (110) Z Propogating
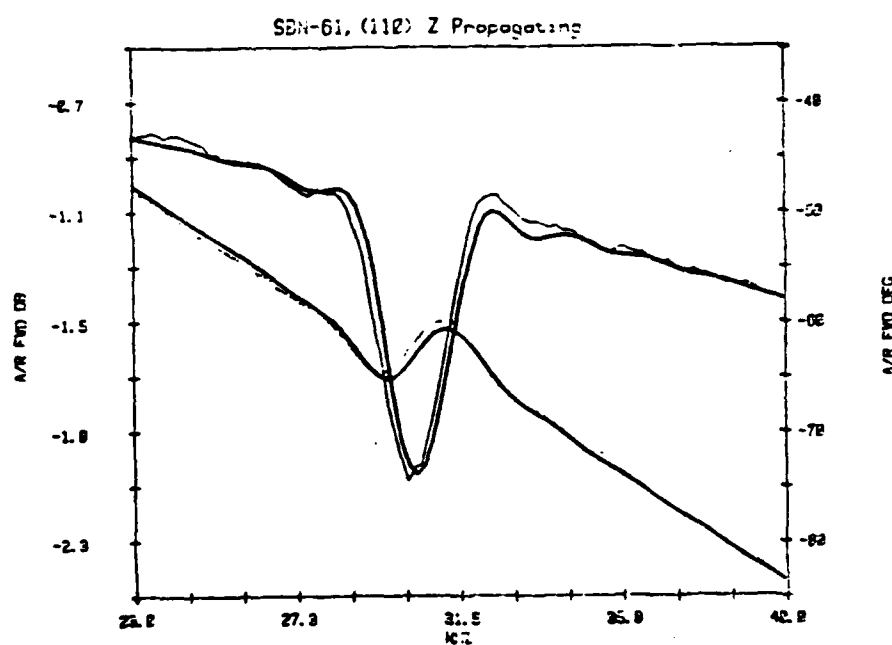
Fig. 26. Comparison between experimental and best fit, crossed-field com-
puter modeling of transducer scattering parameters for (110)-cut,
Z-propagating SAW transducers after temperature cycling.

42

(110)-Cut, Z Propagating SBN-61

$$7\left[1 + \left(\frac{F}{F_o}\right)^3\right]$$

100 nH

1pf

C_{idt} = 65pf
F_o = 30.514MHz
k^2 = 0.005
N = 15

(A)

60 nH

6.3

1pf

1800

R_a

B_a

C_{idt} = 60pf
F_o = 30.514MHz
k^2 = 0.006
N = 15
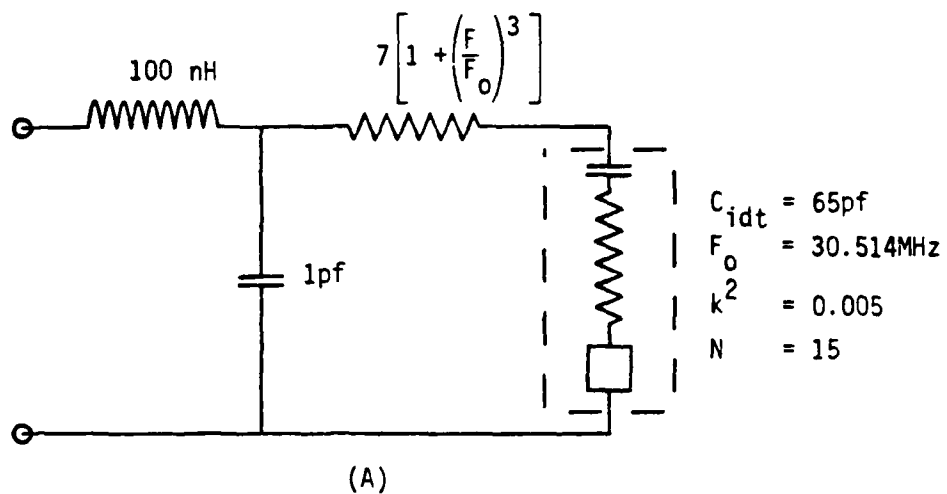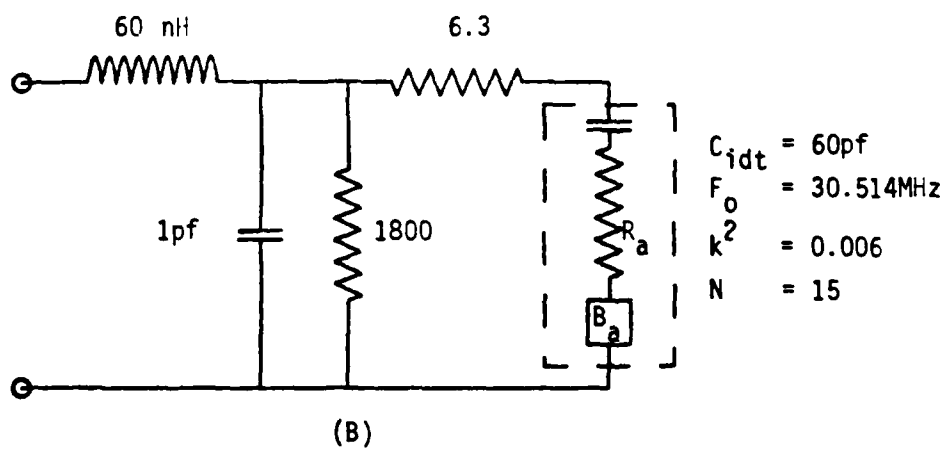
(B)

Fig. 27. SAW transducer equivalent circuit for (110)-cut, Z-propagating transducer (a) before and (b) after temperature cycling.

from transducer scattering parameters was -23.7 dB leaving 17.3 dB due to
acoustic attenuation. This corresponds to a loss of 8.5 dB/cm at 30.5 MHz.
Based on pulse echo and resonance characteristics, the SAW velocity was 3173
m/sec. The piezoelectric coupling was typically 0.006.

3.3 Interdigital Electrode Poling

The tetragonal SBN:61 solid solution has a Curie temperature of appro-
ximately 70°C. Below the Curie temperature, spontaneous polarization along the
c-axis gives rise to piezoelectric coupling terms, d_{31}, d_{33} and d_{15}. Inter-
digital electrode transducers photolithographically defined on the surface are
capable of generating and detecting surface waves as described in the previous
section. However, above the Curie temperature, the solid solution enters the
paraelectric phase where application of an external electric field can be used
to induce polarization and generate acoustic waves. In this section, surface
acoustic wave generation and detection in the paraelectric phase using the spa-
tially varying SAW electrode pattern to pole the crystal is described. This is
the first time such an effect has been observed and may lead to useful and unique
device configurations in the future.

Experimentally, a (110)-cut, Z propagating SBN:61 substrate was used
with 15 finger pair input/output interdigital electrodes. The SBN:61 had pre-
viously been poled and the room temperature delay line insertion loss and trans-
ducer return loss are shown in Figs. 28 and 29. The fundamental frequency of
operation was approximately 42.7 MHz. A large coupling to fulk waves is also
observed at approximately 78 MHz. Raising the temperature to 130°C completely
depoled the SBN:61 and surface waves were no longer generated. However, apply-
ing a dc voltage to the interdigital electrodes through decoupled biasing net-
works induced a net polarization and surface waves were again generated and de-
tected but at approximately twice the original frequency as shown in Figs. 30-31.
The output appears to saturate at approximately 30-40 volts corresponding to an
electric field of approximately 12-15 KV/cm. Alternating the polarity of the
applied dc field also induced a phase reversal of the rf signals as shown in
Fig. 32.
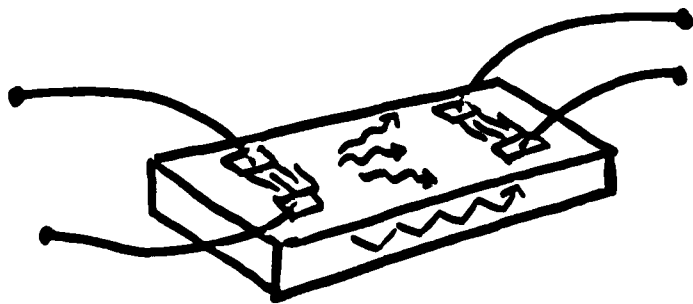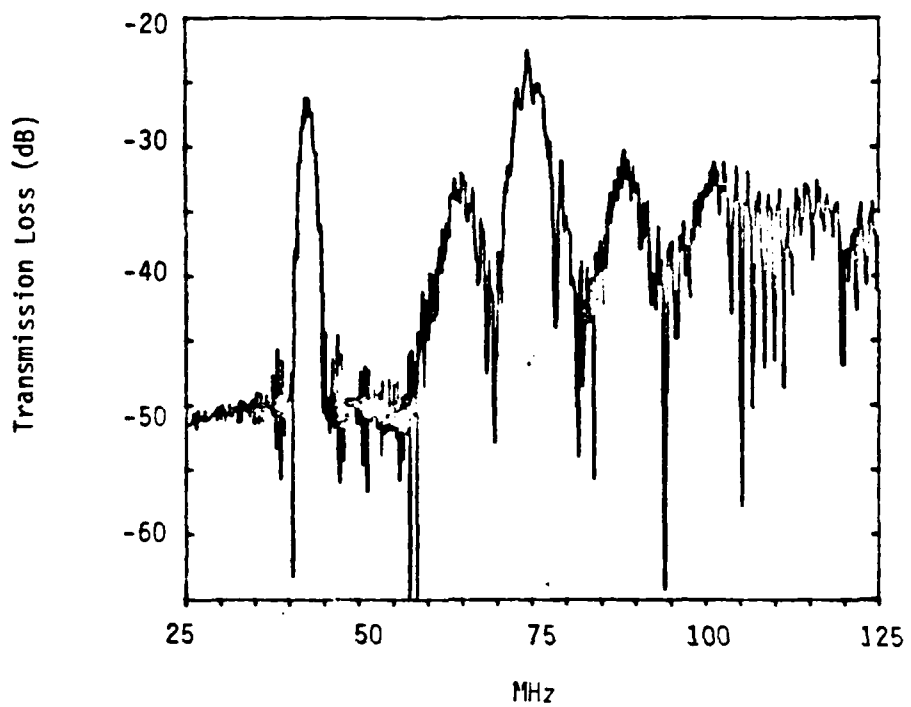
MRDC41007.18AR

Fig. 28. Transmission line response for (110)-cut, Z-propagating delay
line operating in the ferroelectric region and room temperature.

45
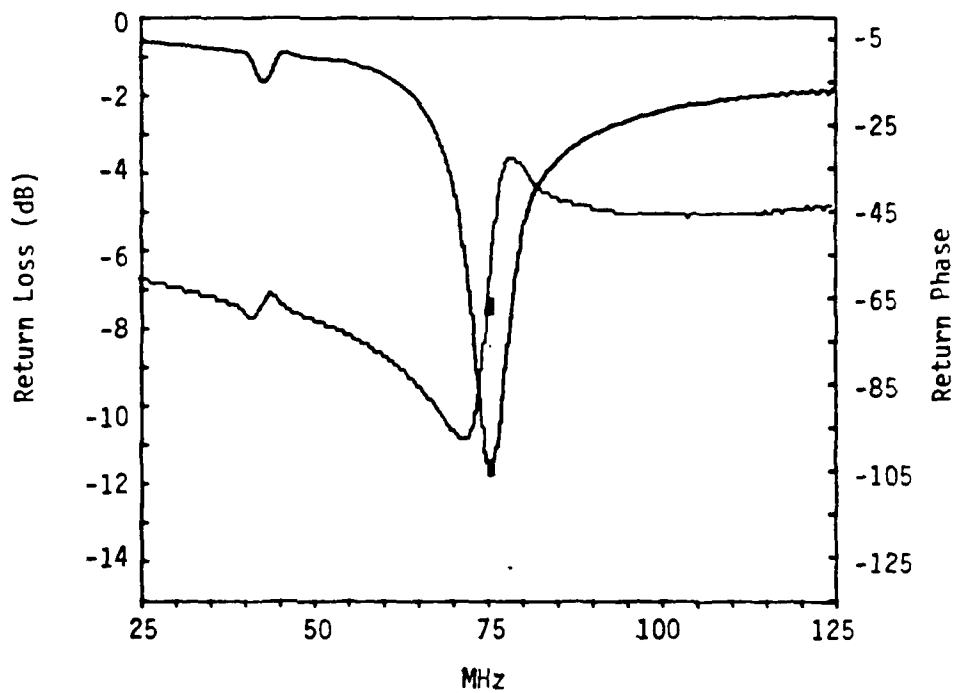
Fig. 29. Experimental transducer scattering parameter amplitude and operating in the ferroelectric region.

46
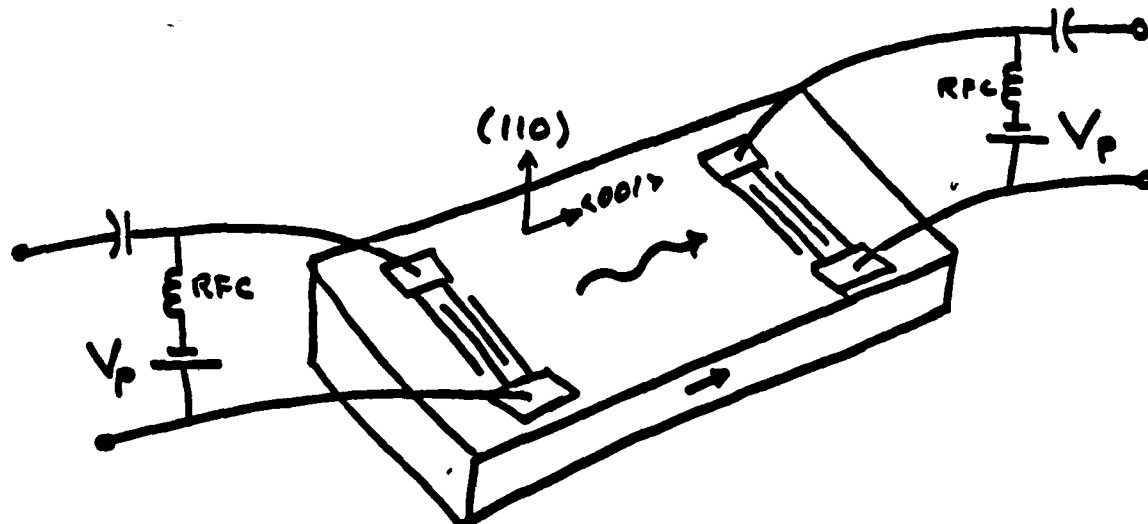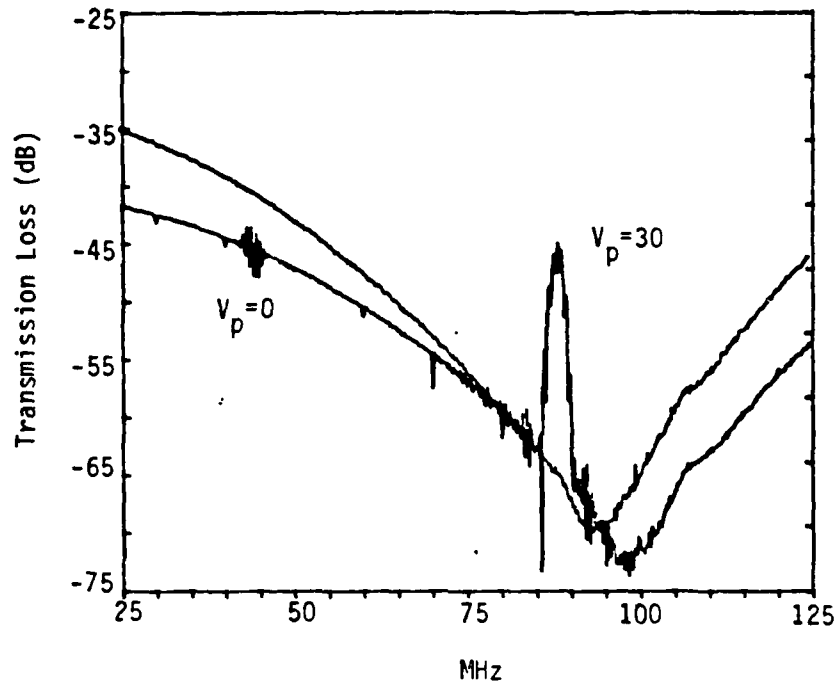
MRDC41007.18AR

Fig. 30. Transmission response for SBN:61 delay line operating in the paraelectric regime with and without polarizing voltage applied.

47
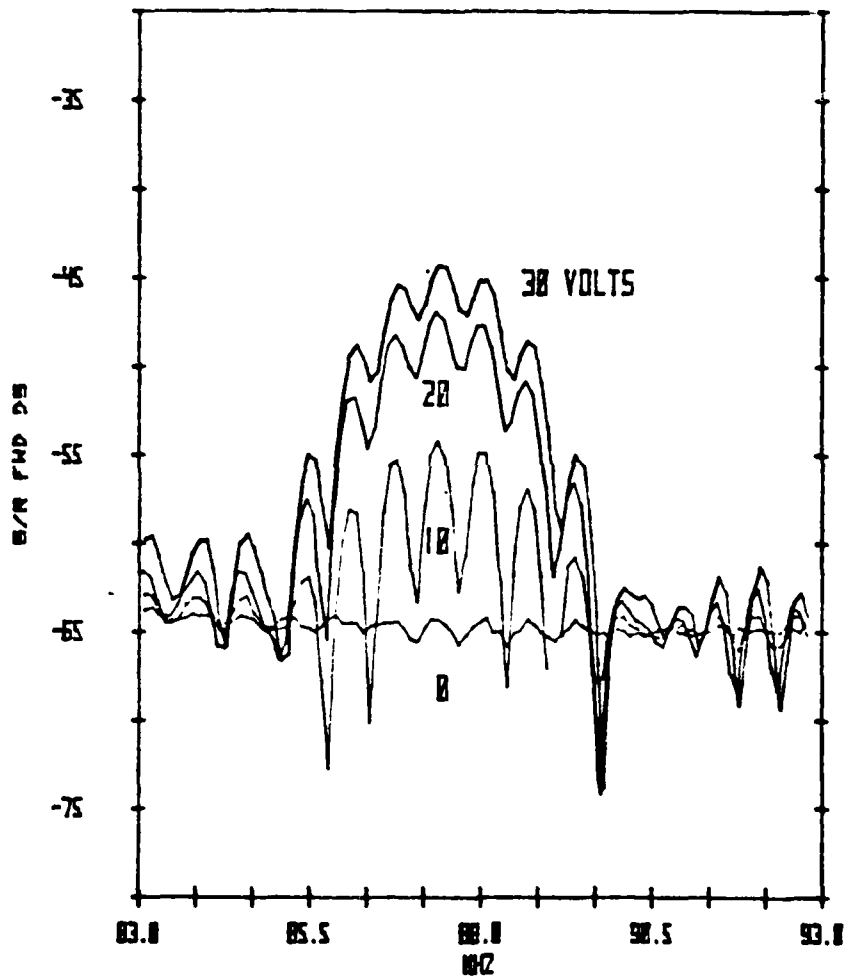
MRDC41007.18AR

Fig. 31. Paraelectric transmission line response for 0, 10, 20 and 30 volts of polarizing field at 130°C.
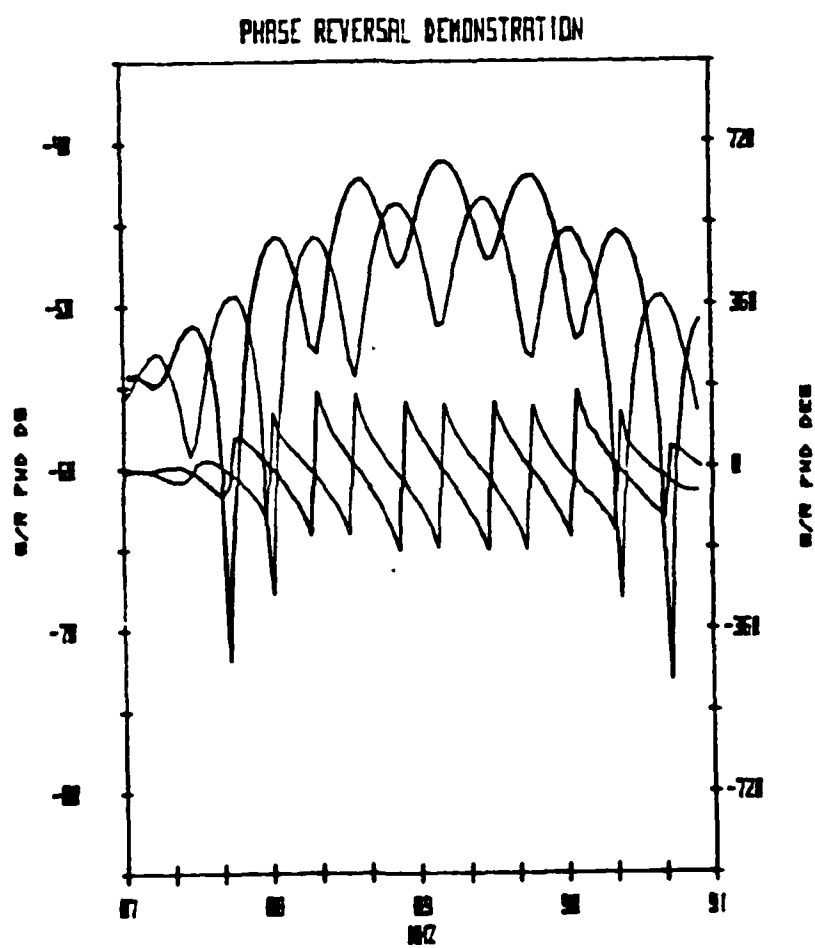
Fig. 32. Paraelectric transmission line amplitude and phase showing the phase reversing properties of the polarizing voltage.

49

This effect might be useful for programmable matched filters where transducer tap amplitude and phase could be controlled by externally applied dc potentials of the proper values. Another application of this effect is to pole films of SBN deposited by liquid phase epitaxy. After returning to room temperature with the dc potential applied, the spatially varying electrode poling is frozen into the material and the transducer continues to operate at the higher frequency and with the appropriate phase. This effect would allow phase coded interdigital transducers to be coded and re-coded by re-poling the electrodes themselves. At the present time, this effect is being studied and quantitative results are being gathered for future analysis.

3.4   Temperature Stability

3.4.1   Stability of Material Properties

The variation of any device configuration can be predicted if the stability of each material property tensor is known. The temperature coefficients of elastic, piezoelectric, dielectric, and thermal expansion have been measured to first order at room temperature. These coefficients are tabulated in Table 4 from Refs. 1-2. Two particularly significant coefficients are s_{44}^D and the z-axis thermal expansion. Both are anomalous in the sense that they are opposite in sign from normal crystal behavior. This type of behavior is needed if temperature compensated cuts for surface or bulk wave resonators are to be found. At the present time, these coefficients are only first order and efforts are underway to obtain the second order coefficients over the temperature range -20 to +50°C. Also, calculations of surface wave velocity variations using these first order coefficients are being completed in an effort to analytically predict temperature compensated cuts.

3.4.2   Temperature Stability of SAW

In order to measure temperature coefficients of time delay surface acoustic waves, delay lines were fabricated on Z, X and (110) cuts of SBN:61. Wave propagation was always along a major axis either X or Z. The temperature

TABLE 4

Temperature Coefficients of Electro-Acoustical
Constants of SBN:61 at Room Temperature

PROPERTY	CONSTANT	TEMPERATURE COEFFICIENT
Thermal Expansion	α_1	$8.0 \times 10^{-6}/°C$
	α_3	-8.0
Dielectric Constants	ϵ_{11}^T	$-4.8 \times 10^{-3}/°C$
	ϵ_{33}^T	-20
Elastic Compliances	S_{11}^D	$-1.2 \times 10^{-1}/°C$
	S_{12}^D	-9.2
	S_{13}^D	-0.63
	S_{33}^D	-5.0
	S_{44}^D	$+2.3$
	S_{66}^D	-0.80
Piezoelectric Constants	d_{31}	$-1.07 \times 10^{-2}/°C$
	d_{33}	-1.23
	d_{15}	-0.80
Coupling Coefficients	k_{31}	$-0.99 \times 10^{-3}/°C$
	k_{33}	-1.36
	k_{15}	-0.02

coefficient of delay was measured by tracking delay line phase and keeping the phase constant by varying the frequency. Frequency was determined by a network analyzer phase locked to a frequency synthesizer. This system provided 0.1° phase resolution. The results were as follows.

3.4.2.1 Z-Cut SBN:61

An experimental plot of frequency and amplitude are shown in Fig. 33. The starting temperature was 25°C and was decreased in 5°C increments until -10°C was reached. A non-linear frequency change (+100 KHz) was observed. The temperature was brought back to room temperature and a 50 KHz hysteresis was observed. The temperature was increased to 50°C in 5°C increments which produced a -50 KHz drop in frequency. Keeping the device at 50°C for approximately one hour produced another -50 KHz frequency change.

The amplitude of the SAW signal also changed approximately 2 dB during the temperature cycling with 1 dB of hysteresis. A maximum in response was observed at approximately room temperature.

Because of the instability in the material (or domains), the temperature coefficient of delay at room temperature varied from -50 ppm/°C to -140 ppm/°C with a non-linear 2nd order characteristic.

3.4.2.2 (110)-Cut, Z Propagating

The starting point for this temperature run was -19°C as shown in Fig. 34. The temperature was increased in 5°C increments up to +50°C as shown. At approximately +10°C, after a -12 KHz change, a sudden drop in frequency occurred. Associated with this, the amplitude began to drop and at +20°C a sudden drop in amplitude was also recorded. Increasing the temperature up to 50°C resulted in a linear drop in frequency, -20 KHz, and amplitude, -4.5 dB. Returning to room temperature, the hysteresis in frequency was 2 KHz and amplitude 1 dB.

The temperature coefficient of delay at room temperature was estimated to be -18 ppm/°C and approximately linear.

Z-Cut, X Propagating SBN-61
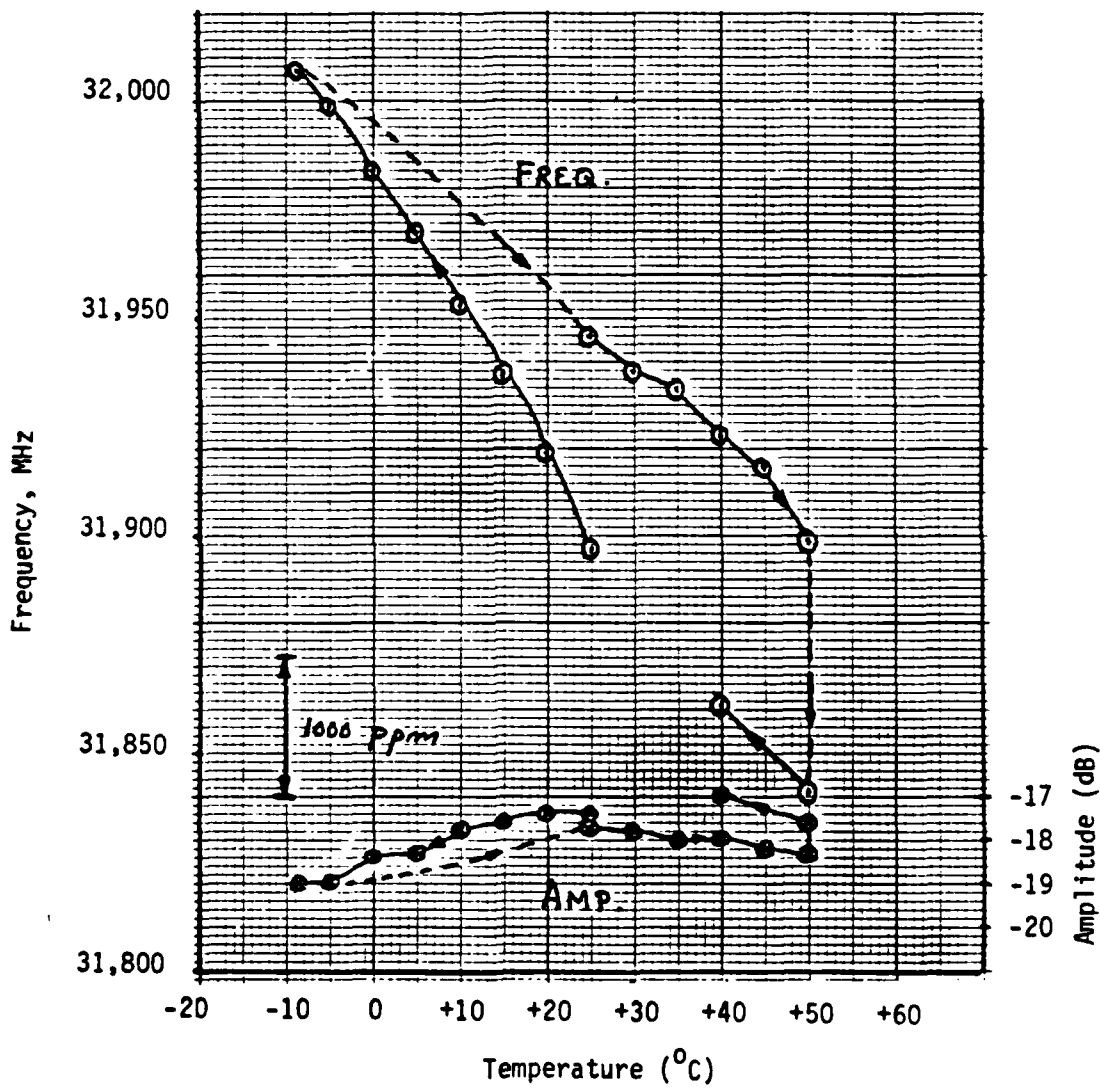
Fig. 33. Experimentally measured Z-cut, X propagating delay line amplitude
and frequency as a function of temperature showing hysteresis
effects.

(110)-Cut, Z Propagating SBN-61
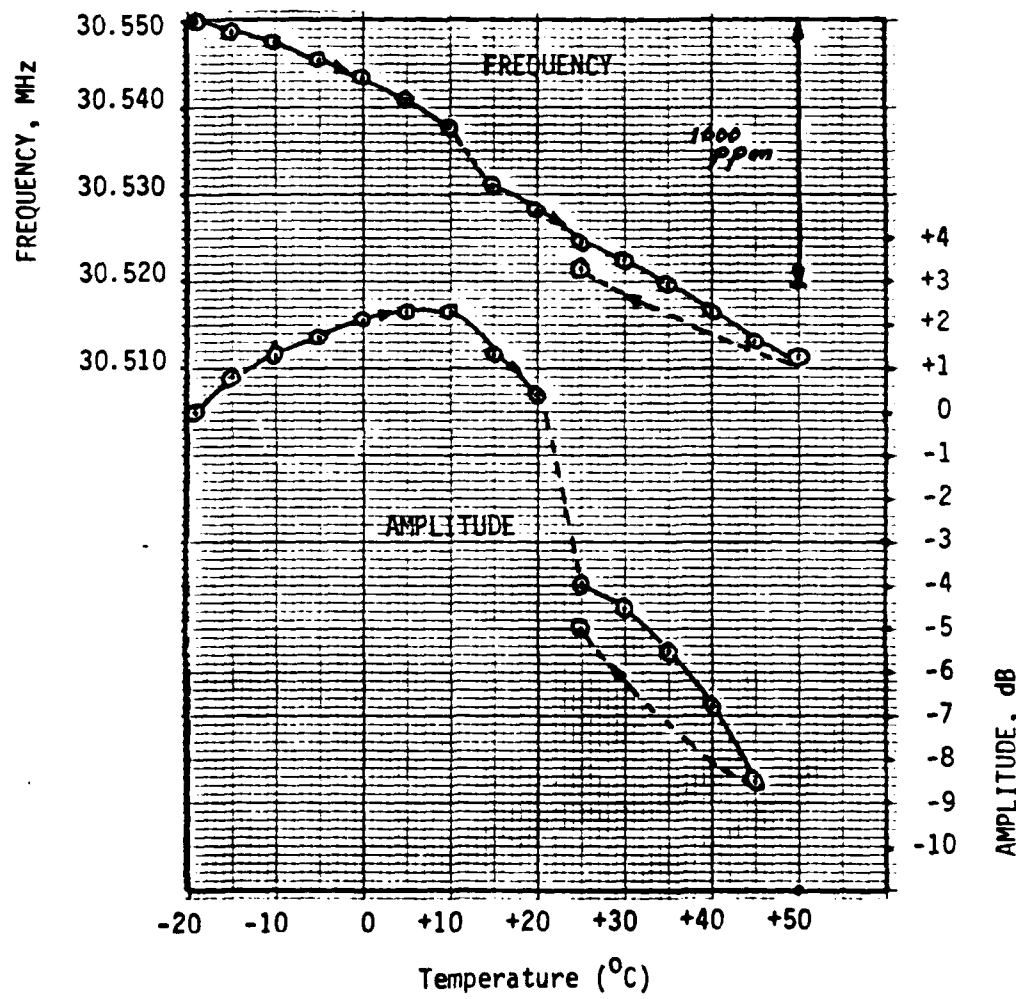
Fig. 34. Experimentally measured (110)-cut, Z propagating delay line amplitude and frequency as a function of temperature showing hysteresis effects.

3.4.2.3 X-Cut, Z Propagating

The starting temperature for a typical temperature cycle of this cut is shown in Fig. 35 to be -15°C. The temperature was increased to +40°C in 5°C increments. A zero temperature coefficient was observed at approximately +10°C; however, the amplitude showed a +7 dB rise with temperature. Hysteresis was observed in the temperature vs. frequency characteristic; however, the overall frequency variation over the range -15°C to +40°C was only 200 ppm. Performing a least squares fit to the frequency data yielded a second order coefficient time delay of 0.229 ppm/°C^2 (ST quartz = 0.03 ppm/°C^2).

Temperature Stability SBN-61
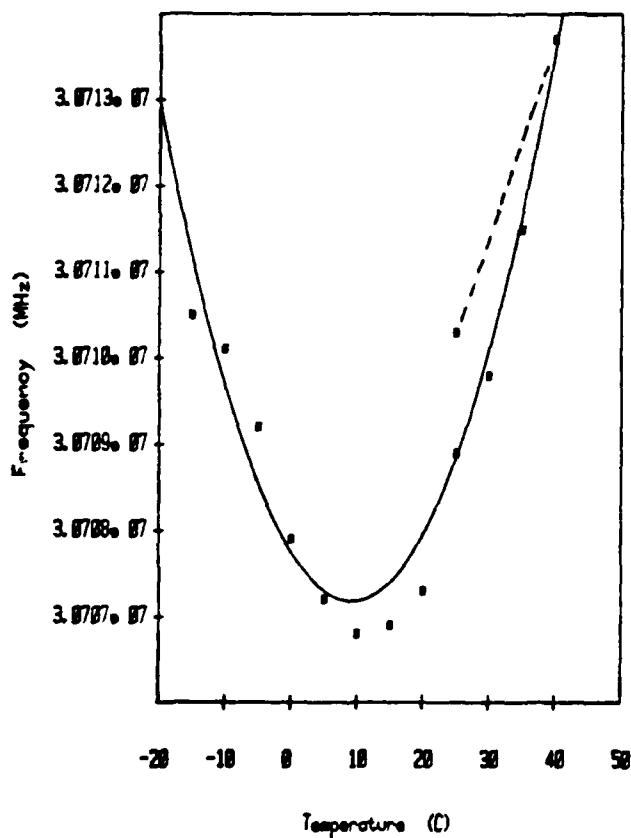
Temperature Stability SBN-61
X-Cut, Z Propagating
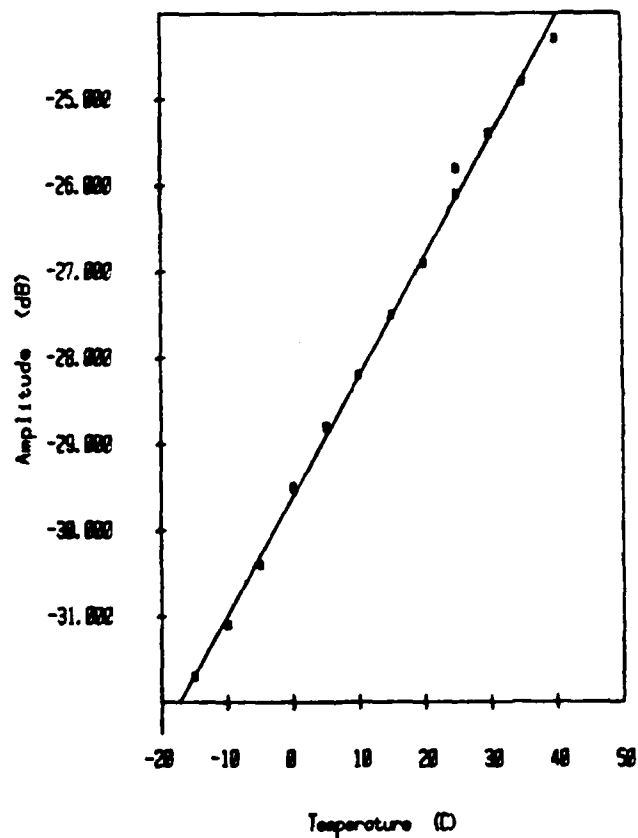
Fig. 35. Experimentally measured X-cut, Z propagating delay line amplitude
and frequency as a function of temperature showing hysteresis
effects.

## 4.0 LPE GROWTH OF THE $Sr_{1-x}Ba_xNb_2O_6$ BRONZE COMPOSITION

During the past year, extensive efforts have been made to develop the LPE growth technique for the $Sr_{1-x}Ba_xNb_2O_6$, $0.25 \leqslant x \leqslant 0.75$, composition onto the $Sr_{.61}Ba_{.39}Nb_2O_6$ substrates. The $Sr_{.61}Ba_{.39}Nb_2O_6$ bulk single crystals obtained by the Czochralski technique are sufficiently large to initiate the LPE work; also, lattice mismatch between the bulk single crystals and other SBN compositions is very minimal. Table 5 summarizes the fundamental properties for various compositions on the $SrNb_2O_6$-$BaNb_2O_6$ system. By changing SBN film compositions, it will be possible to optimize physical properties such as electromechanical coupling, and dielectric, piezoelectric, and elastic constants for this solid-solution system. Based on this information, it will be possible to choose a suitable composition for surface acoustic wave device applications.

Recently, Adachi et al.[3-5] also reported the successful thin film growth of the $K_3Li_2Nb_5O_{15}$ composition onto the bronze composition $K_2BiNb_5O_{15}$ substrates by the EGM, LPE and rf sputtering techniques. For substrates, $K_2BiNb_5O_{15}$ single crystals grown by the Czocrhalski technique were used because of the following reasons: both the $K_3Li_2Nb_5O_{15}$ and $K_2BiNb_5O_{15}$ phases belong to the same tungsten bronze type structure; the melting point of $K_2BiNb_5O_{15}$ is higher than $K_3Li_2Nb_5O_{15}$ by about 250°C; and the lattice mismatch between $K_3Li_2Nb_5O_{15}$ and $K_2BiNb_5O_{15}$ is about 0.32% and 2.3% for the a and c parameters in the $K_3Li_2Nb_5O_{15}$ coordinates. The films obtained were transparent and of excellent quality.

4.1   Solvents for Tungsten Bronze Family Compositions

Crucial to the success of this isothermal growth is an ability to supercool the solution without the occurrence of spontaneous nucleation. It is therefore necessary, before LPE can be performed, to find a suitable flux system (solvent) for each chosen bronze composition. Although a large number of solvents have been identified for this family, the choice in the proposed research is restricted to only the vanadium-containing solvents. Based on our work on the ferroelectric $LiNbO_3$ thin film growth[6-11] and the preliminary

TABLE 5

Fundamental Properties of SBN Compositions

Physical Constants	$Sr_{.5}Ba_{.5}Nb_2O_6$	$Sr_{.61}Ba_{.39}Nb_2O_6$	$Sr_{.75}Ba_{.25}Nb_2O_6$
Symmetry	Tetragonal	Tetragonal	Tetragonal
Lattice Constants	$a = 12.470$	$a = 12.452\text{Å}$	$a = 12.438\text{Å}$
	$c = 3.946$	$c = 3.938\text{Å}$	$c = 3.917\text{Å}$
Curie Temperature	$125°C$	$72°C$	$56°C$
Dielectric Const.	$\epsilon_{33} = 400$	$\epsilon_{33} = 880$	$\epsilon_{33} = 3000$
Electromechanical Coupling Constants	$k_{33} = 0.48$ $k_{31} = 0.137$ $k_{15} = \text{---}$	$k_{33} = 0.475$ $k_{31} = 0.14$ $k_{15} = 0.24$	--- --- ---
Piezoelectric Constants	$d_{31} = -18$ $d_{33} = 95$	$d_{31} = -30$ $d_{33} = 130$	--- ---

work on the bronze compositions, it has been found that the vanadium-containing solvents are useful for the bronze compositions because of the following reasons:

(a) V^{5+} cation has strong preference for the 4-fold coordinated site, and hence no vanadium inclusion in the bronze structure is expected,

(b) Supercooling range for the V^{5+}-containing solvents is reasonably high, of the order of $20°$ to $40°C$.

(c) V^{5+}-containing solvents melt at significantly low temperatures and thus allow LPE growth at much lower temperatures.

(d) V^{5+}-containing solvents are remarkably stable at elevated temperatures,

(e) All $^{+}$-containing solvents dissolve in water or dilute acids.

As summarized in Table 6, essentially all the vanadium-containing solvents have been shown to be useful not only for $Sr_{1-x}Ba_xNb_2O_6$, but also for other important bronze compositions, e.g., $Sr_2KNb_5O_{15}$, $K_3Li_2Nb_5O_{15}$, $Pb_{1-x}Ba_xNb_2O_6$ and $Pb_{1-2x}K_xM^{3+}_xNb_2O_6$, M = Bi or La. Since all the bronze compositions are multicomponent systems, the determination of a complete phase diagram in this situation is impractical. As described by Roy and White[12], this problem in this study has been simplified by treating a multicomponent assemblage as a pseudobinary system, as shown in Fig. 36 for the BaV_2O_6-$Sr_{.5}Ba_{.5}Nb_2O_6$. The information obtained from this partial phase diagram is found to be adequate to initiate the LPE thin film growth studies. All necessary data concerning the temperature and compositional boundaries over which $Sr_{1-x}Ba_xNb_2O_6$ crystallites were established by x-ray diffraction powder and DTA techniques.

As discussed in our earlier reports, the mixture containing 70 mole% BaV_2O_6 and 30 mole% $Sr_{.5}Ba_{.5}Nb_2O_6$ has been used, since this assemblage produces the bronze phase having composition close to $Sr_{.5}Ba_{.5}Nb_2O_6$. This composition melts at relatively low temperature ($\sim 950°C$), which made it possible to produce the films of excellent quality with minimum structural defects. The detailed experimental procedure has already been given in our earlier reports. During the past year, the efforts were directed toward examining the growth

TABLE 6

Solvents for the Tungsten Bronze Compositions

Composition	Solvent	M.P. (°C)	Supercooling Range* (°C)	Crystallization Range	Lattice Constants $a_{\text{Å}}$	$c_{\text{Å}}$
$Sr_{1-x}Ba_xNb_2O_6$**	BaV_2O_6	700	30	Long and useful		
	SrV_2O_6	740	--	Long and useful	12.435 to 12.485	3.951 to 3.975
$Sr_2KNb_5O_{15}$	KVO_3	540	40	Long and useful	12.473	3.940
	$SrV_2^3O_6$	740	--	Long and useful		
$K_3Li_2Nb_5O_{15}$	$LiVO_3$	610	40	Short and useful	12.580	4.015
	KVO_3	540	--	Short and useful		
$Pb_{1-x}Ba_xNb_2O_6$	$Pb_2V_2O_7$	680	--	--	12.462 to 12.485	3.945 to 3.982
$Pb_{1-2x}K_xLa_xNb_2O_6$**	$Pv_2V_2O_7$	610	--	--	12.470 to 12.515	3.910 to 3.951

* Supercooling range was established in these samples by the DTA method.

**Lattice constants are given for the entire tetragonal solid solution. Lattice constants for the $Sr_{.61}Ba_{.39}Nb_2O_6$ single crystals are: a = 12.463Å and c = 3.939Å.

MRDC79-7148A
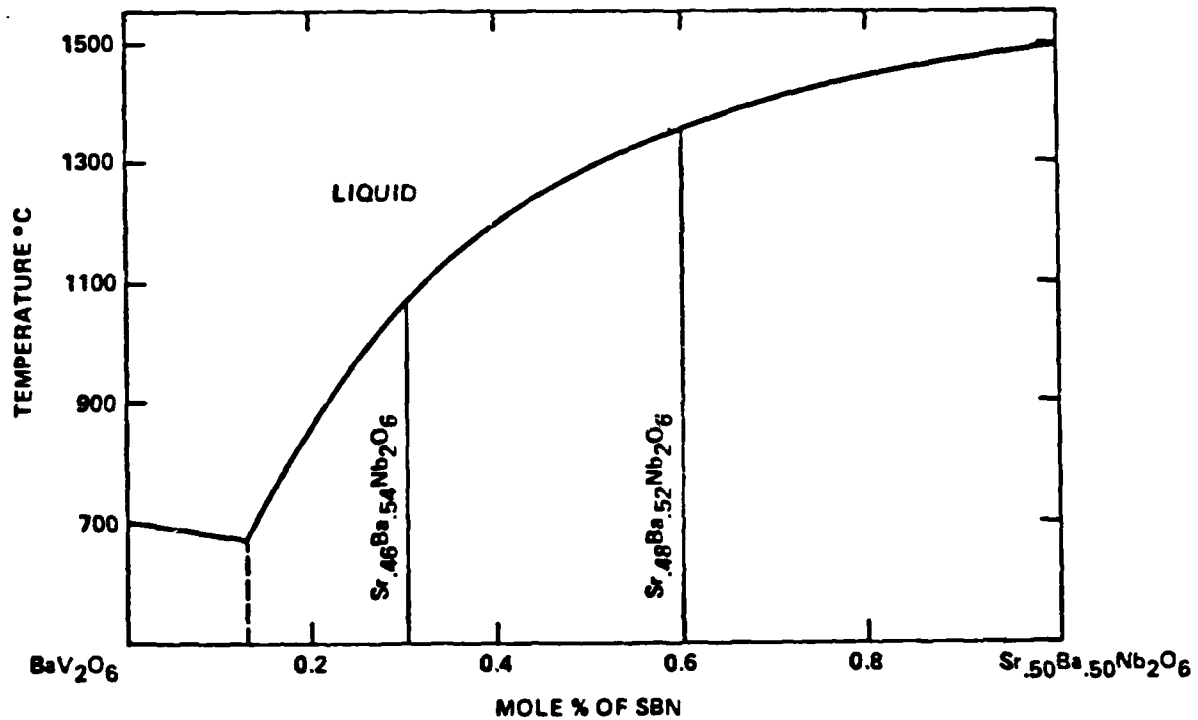
Fig. 36. Pseudo-binary phase diagram for the BaV_2O_6-$Sr_{.5}Ba_{.5}Nb_2O_6$ system in air.

of this composition on various other crystallographic orientations such as
(100), (110), (111) and (001). The results of this investigation indicate
that the LPE growth of SBN composition has been successful on all the direc-
tions; however, it has been shown that the growth is much faster on the (001)
plate. This is consistent with our observation on the bulk single crystal
growth of the $Sr_{.61}Ba_{.39}Nb_2O_6$ composition, where growth was only possible along
the (001) direction. Figure 37 shows a typical cross-section of the SBN film
grown onto the (100) plane; thickness of the film is approximately 25 μm. By
using this technique, it was possible to grow films as thick as 50 to 60 μm,
which is a significant accomplishment in the present work.

4.2   Characterization of Films

The thin films have been characterized by a variety of techniques.
Lattice constants and compositional homogeneity were established by the various
x-ray diffraction powder techniques. The Laue, Deby-Scherrer, and x-ray topo-
graphy methods were also employed to orient and analyze the grown films.

The crystallinity and lattice constants, $a_{\text{Å}}$ and $c_{\text{Å}}$, of various new
films and substrates were determined by using the (100), (110) and (001) reflec-
tions. As shown in Fig. 38, the reflections (001) and (002) for the Z-plate,
(100), (200), (400), (800), etc. for the X-plate, and (110), (220), (440),
(880), etc. for the XY-plate, have been identified. By using these reflections,
it was possible to check and confirm the film growth and lattice constants for
the grown films. A typical intensity vs. film thickness plot is given for the
reflection (002) in Fig. 39. Two peaks corresponding to $CuK_{\alpha 1}$ and $K_{\alpha 2}$ represent
the $Sr_{.61}Ba_{.39}Nb_2O_6$ substrates, while the film position is denoted by $CuK'_{\alpha 1}$
and $K'_{\alpha 2}$. This result clearly shows that the intensity of the substrate reflec-
tion $CuK_{\alpha 1}$ and $K_{\alpha 2}$ reduced significantly with increasing the film thickness and,
finally, completely disappeared when the thickness was over 10 μm. By using
these reflections corresponding to (001), (100) and (110), the lattice constants
$a_{\text{Å}}$ and $c_{\text{Å}}$ were established and compared with the lattice constants reported for
the $Sr_{1-x}Ba_xNb_2O_6$ solid solution system. Based on this result, it has been
established that the composition of the film is approximately $Sr_{.46}Ba_{.54}Nb_2O_6$,

MRDC78-3045

FILM (20μm)
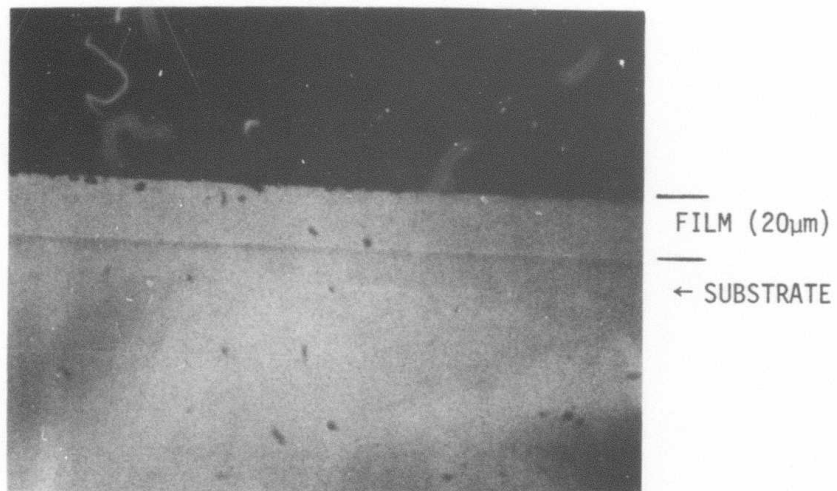
← SUBSTRATE

Fig. 37   Shows a typical cross-section of the $Sr_{.5}Ba_{.5}Nb_2O_6$ film on the X-cut SBN:61 substrate.
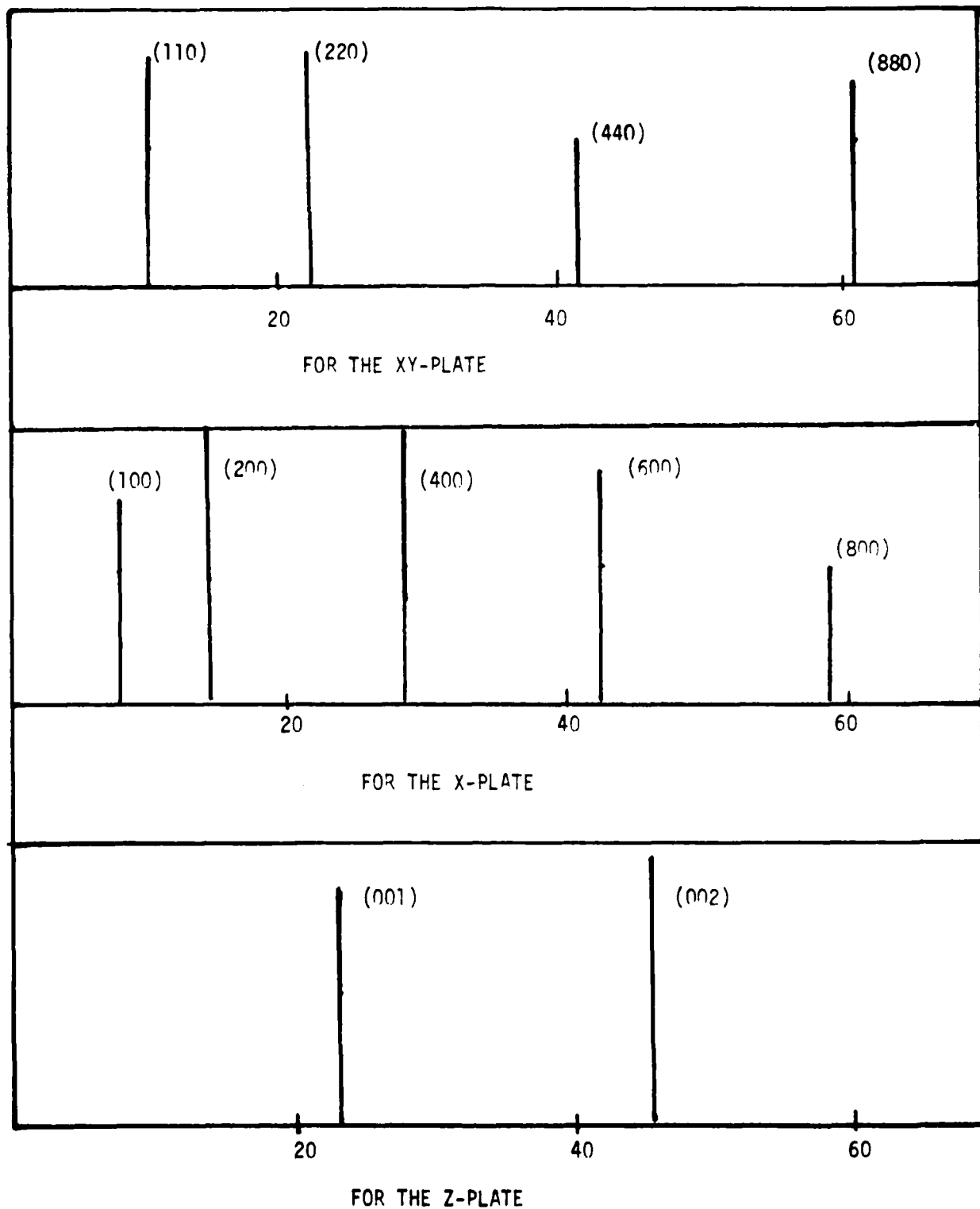
MRDC41007.18AR

Fig. 38.   Number of reflections for each orientation of SBN single crystal.

64

MRDC41007.18AR

SC79-4451

(a) **SUBSTRATE**

(b) **SUBSTRATE + FILM (5μm)**

(c) **SUBSTRATE + FILM (8μm)**

(d) **SUBSTRATE + FILM (15μm)**
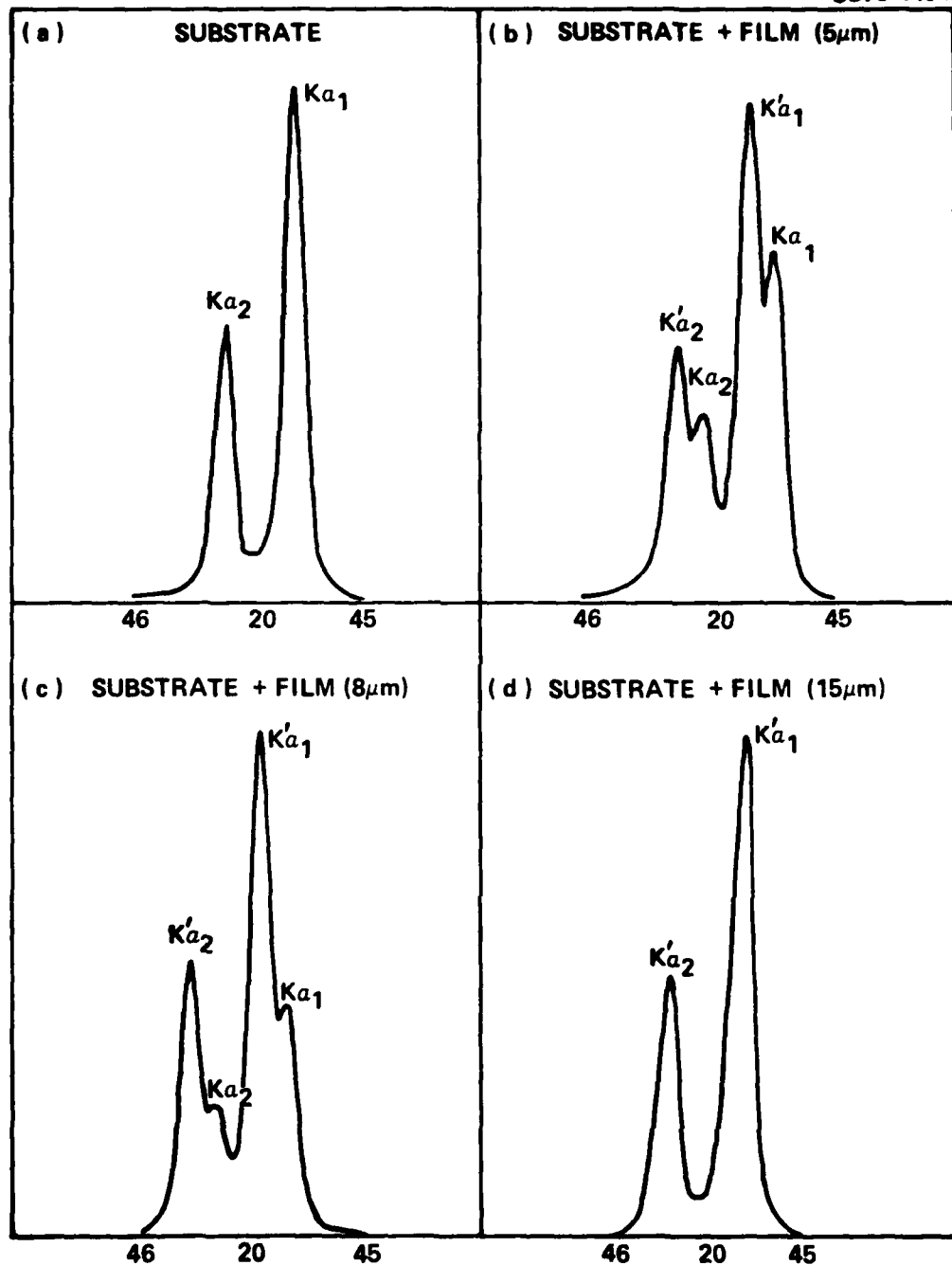
Fig. 39. X-ray diffraction peak taken for substrate/film.

65

which is close to starting composition $Sr_{.5}Ba_{.5}Nb_2O_6$.

The films thus grown in the present work are sufficiently large ($\sim 2 \times 10$ cm) to initiate the acoustical and ferroelectric measurements. According to work reported by Ballman et al.[13], the T_c for this composition $Sr_{.46}Ba_{.54}Nb_2O_6$ is around $130°C$, which is substantially higher than that of the substrate material $Sr_{.61}Ba_{.39}Nb_2O_6$ ($72°C$). It is therefore important in the present work to pole all the films below this temperature. The poling technique for the $Sr_{.61}Ba_{.39}Nb_2O_6$ has already been established and is discussed in our earlier reports. Since the Curie temperatures for the film and substrate are slightly different, there should be no major problems in obtaining poled SBN films. We expect that during the next six months, it will be possible to accomplish this task and to obtain necessary acoustical and ferroelectric data on these new bronze films. Based on this information, it will be possible to change the film composition to obtain desired acoustical properties within the bronze family,

5.0 OPTICAL PROPERTIES OF SBN SINGLE CRYSTALS

Strontium barium niobate ($Sr_{1-x}Ba_xNb_2O_6$) is a ferroelectric solid solution with tungsten bronze structure that has lately become of major interest in optoelectronic device applications, because compositions on this system have the largest electro-optic[14] and pyroelectric coefficients[15] of any well-behaved material. Furthermore, much attention is now being paid to this material becuase it has great potential as a reversible optical storage medium controlled by an external electric field[16].

During the past six months, efforts have been made to evaluate the optical propertie⁻ of $Sr_{.61}Ba_{.39}Nb_2O_6$ single crystal at the Optical Techniques Branch of the Naval Research Laboratory. The crystal supplied for this task by Rockwell had dimensions approximately 5 mm x 2.8 mm x 2.8 mm, with c-axis along the long dimension. The a- and b-faces were polished, and metal electrodes used for poling the crystal were on the c-face. When an a- or b-face of the crystal was illuminated to normal incidence with a collimated HeNe laser beam, and the transmitted beam was imaged with a lens, a diffraction pattern was observed. It was deduced from the orientation and periodicity of the diffraction pattern that the refractive index varies periodically along the c-axis in the crystal, with a periodicity of about 20 μm. Since only one crystal has been examined in detail, it is difficult, at present, to assess the crystal quality. During the next six months, efforts will be made to examine several crystals from the different boules to characterize precisely the optical properties.

In order to measure the electro-optic properties of the material, an 80 Hz saw-tooth voltage was applied to the electrodes to phase-modulate the polarized laser beam. A typical oscilloscope photograph, showing the modulating waveform and power transmitted through an analyzer, is shown in Fig. 40. The excitation ratio is about 50%; this low value is probably due to the depolarizing *effect of light scattering* in the material. The peak-to-peak voltage is 2000 V. From these data, the half wave voltage for the $Sr_{.61}Ba_{.39}Nb_2O_6$ single crystal is estimated to be 300 V, about a factor of 10 less than for $LiNbO_3$ or $LiTaO_3$.

MRDC81-14087
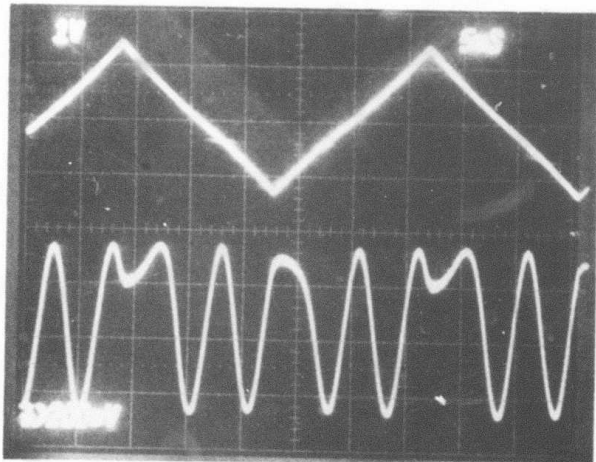
Fig. 40 Electro-optic modulation in SBN:61.

This clearly indicates that the SBN material is superior when compared to existing materials like $LiNb_3$ or $LiTaO_3$.

6.0 FUTURE PLANS

6.1 Application of Phenomenological Model

Based on the phenomenological analysis on the tungsten bronze family, it has been shown that the sixth order electrostriction constants Φ_{ijklmn} play an important role in studying the elastic behavior in the single domain ferroelectric phase. This work will be continued to obtain more information on the tungsten bronze family.

6.2 Piezoelastic Measurements

All of the piezoelastic tensor elements of the material SBN:61 have been evaluated using appropriate resonator geometries. For future work, it has been planned that more detailed studies be conducted with the 2nd order coefficients with respect to temperature over the range -20 to +50°C. In addition, the stability of the SBN crystals at a constant temperature will be evaluated. Based on this extensive work, changes in composition or in growth technique may be undertaken.

6.3 Materials Preparation and Acoustical Characterization

The liquid phase epitaxial (LPE) technique has been shown to be successful for developing the $Sr_{.5}Ba_{.5}Nb_2O_6$ films onto the various crystallographic orientations such as (100), (110) and (001) of $Sr_{.61}Ba_{.39}Nb_2O_6$. During the next six months, efforts will be made to establish the poling technique for the tungsten bronze films. Once this is accomplished, it is planned to evaluate their acoustical properties, specifically the temperature coefficient of SAW velocity. Since another bronze composition, $Sr_2KNb_5O_{15}$, has higher curie temperature (160°C), efforts will be made to grow this composition onto the SBN substrates.

6.4   Electro-optic Measurements

Optical measurements will be continued to determine the half-wave voltage for the different boules of $Sr_{.61}Ba_{.39}Nb_2O_6$ single crystals. Once this task is accomplished, efforts to grow optical quality SBN single crystals will be made.

7.0 PUBLICATIONS AND PRESENTATIONS

7.1 Publications

1. R. R. Neurgaonkar, T. C. Lim, E. J. Staples and L. E. Cross, "An Exploration of the Limits of Stability of the $LiNbO_3$ Structure Field with A and B Site Cation Substitutions, Ferroelectrics," Vol. 27-28, (1980), 63-66.

2. K. L. Keester, R. R. Neurgaonkar, T. C. Lim and E. J. Staples, "Strontium Metaniobates: Its Crystallography, Polimorphism and Isomorphism," Mat. Res. Bull. $\underline{15}$, 821 (1980).

3. R. R. Neurgaonkar, M. H. Kalisher, T. C. Lim, E. J. Staples and K. L. Keester, "Czochralski Single Crystal Growth of $Sr_{61}Ba_{39}Nb_2O_6$ for Surface Acoustic Wave Devices," Mat. Res. Bull. $\underline{15}$, 1235 (1980).

4. L. E. Cross, R. Betch, H. McKinstry, T. Shrout and R. R. Neurgaonkar, "A New Method for Predicting the Temperature Dependence of Elastic Compliance in Simple Proper Ferroelectrics," Proceedings of Frequency Control Symposium, 25-33, 1980.

5. R. R. Neurgaonkar and W. K. Cory, "Structural and Dielectric Properties of $Ba_6Ti_2Nb_8O_{30}$ Type Tungsten Bronze Compositions," (in preparation).

6. R. R. Neurgaonkar, T. C. Lim, E. J. Staples and L. E. Cross, "Crystal Chemistry of Ferroelectric Materials for SAW Devices," Proceedings of Ultrasonic, 410, 1980.

7. T. R. Shrout, L. E. Cross, P. Moses, H. A. McKinstry and R. R. Neurgaonkar, "A Phenomenological Theory for Predicting the Temperature Dependence of Elastic, Dielectric and Piezoelectric Properties in Simple Proper Ferroelectric Crystals", Proceedings of Ultrasonics, 414, 1980.

8. R. R. Neurgaonkar, W. K. Cory and L. E. Cross, "Structural and Ferroelectric Properties of the Phase $Pb_{1-2x}K_xM_x^{3+}Nb_2O_6$, M = La or Bi, submitted to Mat. Res. Bull.

9. R. R. Neurgaonkar, W. K. Cory, W. W. Ho, W. F. Hall and L. E. Cross, "Tungsten Bronze Family Crystals for Acoustical and Dielectric Applications," will be submitted to Ferroelectrics Journal.

10. E. J. Staples and R. R. Neurgaonkar, "SAW Transduction and Poling in Ferroelectric Strontium Barium Niobate", will be submitted to Ferroelectrics Journal.

11. T. R. Shrout, L. E. Cross, P. Moses, H. A. McKinstry and R. R. Neurgaonkar, "Higher Order Electrostriction in Ferroelectric Tungsten Bronzes", will be submitted to Ferroelectrics Journal.

7.2 Presentations

1. R. R. Neurgaonkar, T. C. Lim, E. J. Staples and L. E. Cross, "An Exploration of the Limits of Stability of the $LiNbO_3$ Structural Field with A and B Site Cation Substitutions," Presented at the IEEE Int. Symposium of Ferroelectrics, Minneapolis, MN, June 13-15, 1979.

2. K. L. Keester, R. R. Neurgaonkar, T. C. Lim and E. J. Staples, "Conoscopic Characterization of Czochralski Grown Strontium-Barium Niobate Boules", Presented at the 4th Conference on Crystal Growth, Stanford Sierra Camp, Fallen Leaf, California, May 16-18, 1979.

3. L. E. Cross, R. Betch, H. McKinstry, T. Shrout and R. R. Neurgaonkar, "A New Method for Predicting the Temperature Dependence of Elastic Compliance in Simple Proper Ferroelectric," Presented at the 34th Annual Symposium on Frequency Control, Philadelphia, PA, May 28-30, 1980.

4. R. R. Neurgaonkar, T. C. Lim, E. J. Staples and L. E. Cross, "Crystal Chemistry of Ferroelectric Materials for SAW Devices," Presented at the Annual Ultrasonic Symposium, Boston, MA, Nov. 1980.

5. T. R. Shrout, L. E. Cross, P. Moses, H. A. McKinstry and R. R. Neurgaonkar, "A Phenomenological Theory for Predicting the Temperature Dependence of Elastic, Dielectric and Piezoelectric Properties in Simple Proper Ferroelectric Crystals," presented at the Annual Ultrasonic Symposium, Boston, MA, Nov. 1980.

6. R. R. Neurgaonkar, W. K. Cory, W. W. Ho, W. F. Hall and L. E. Cross, "Tungsten Bronze Family Crystals for Acoustical and Dielectric Applications", Will be presented at the 5th International Meeting on Ferroelectricity, State College, PA, August 17-21, 1981.

7. R. R. Neurgaonkar, W. K. Cory, T. C. Lim and L. E. Cross, "Solid Solution Based on Ferroelectric $Pb_{1-2x}K_xLa_xNb_2O_6$," Presented at the 83rd Annual Conference of American Ceramic Society, Washington, D.C., May 4-6, 1981.

8. E. J. Staples and R. R. Neurgaonkar, "SAW Transduction and Poling in Ferroelectric Strontium Barium Niobate", Will be presented at the 5th International Meeting on Ferroelectricity, State College, PA, August 17-21, 1981.

9. T. R. Shrout, L. E. Cross, P. Moses, H. A. McKinstry and R. R. Neurgaonkar, "Higher Order Electrostriction in Ferroelectric Tungsten Bronzes", will be presented at the 5th International Meeting on Ferroelectricity, State College, PA, August 17-21, 1981.

REFERENCES

1. T. R. Shrout, L. E. Cross, P. Moses, H. M. McKinstry and R. R. Neurgaonkar, Ultrasonic Symposium Proceedings, 414-419, 1980.

2. R. R. Neurgaonkar, Semi-annual Technical Report #3, Contract No. F49620-78-C-0093, January, 1981.

3. M. Adachi and M. Hori, Jap. J. Appl. Phys. $\underline{8}$, 1637 (1979).

4. M. Adachi, M. Hori, T. Shiosaki and Wawabata, Proceedings of the Second Meeting on Ferroelectric Materials and Their Applications, 173 (1979).

5. M. Adachi, T. Shiosaki and A. Kawabata, Jap. J. Appl. Phys. $\underline{18}$, 193 (1979).

6. E. J. Staples, R. R. Neurgaonkar and T. C. Lim, Appl. Phys. Lett. $\underline{32}$, 197 (1978).

7. R. R. Neurgaonkar, M. H. Kalisher, E. J. Staples and T. C. Lim, Proc. Ultrasonics Symposium, 598 (1979).

8. R. R. Neurgaonkar, M. H. Kalisher, E. J. Staples and T. C. Lim, Appl. Phys. Lett. $\underline{35}$, 606 (1979).

9. R. R. Neurgaonkar, T. C. Lim, E. J. Staples and L. E. Cross, Ferroelectrics $\underline{27\text{-}28}$, 63 (1980).

10. R. R. Neurgaonkar, T. C. Lim, E. J. Staples and L. E. Cross, Proc. of Ultrasonics Symposium, 410 (1980).

11. R. R. Neurgaonkar and E. J. Staples, to appear in J. Crystal Growth.

12. R. Roy and W. B. White, J. Cryst. Growth $\underline{33}$, 314 (1968).

13. A. A. Ballman and H. Brown, J. Cryst. Growth $\underline{1}$, 311 (1967).

14. P. L. Lenzo, E. G. Spencer and A. A. Ballman, Appl. Phys. Lett. $\underline{11}$, 23 (1967).

15. A. M. Glass, J. Appl. Phys. $\underline{40}$, 4699 (1969).

16. F. Micheron, C. Mayeux and J. C. Trotier, Appl. Optics $\underline{13}$, 913 (1974).